Zachary Fasnacht
Science Systems and Applications, Inc.
10210 Greenbelt Rd. Lanham, MD 20706 USA

October 11, 2019

Dear Dr. Wang,

Please find enclosed an updated manuscript titled ‘A geometry-dependent surface Lambertian-equivalent reflectivity product for UV/Vis retrievals: Part 2: Evaluation over open ocean’ along with responses to reviewers comments. We made some changes to the manuscript in response to the reviewer’s comments which are highlighted in a typeset latex difference document along with a list of changes provided here.

Both reviewers have asked some thought provoking questions in regards to the evaluation of GLER. We have addressed their concerns in making some minor changes and updates to the paper. We believe that doing so has only strengthened the conclusions made with this work. We greatly appreciate the reviewers’ efforts and suggestions which have helped improve this paper.

Kind Regards,

Zachary Fasnacht

# List of Changes

Title:

- Made a minor update changing *Part II.* to *Part 2:* in order to be consistent with the syntax of our first paper

Section 2.4 Ancillary Data for Water Model:

- Pg 5 Line 26: Fixed typo, AMSRE-E should be AMSR-E

Section 2.6 OMI Data and Selection Criteria

- Pg 7 Lines 19-24: We added a paragraph further explaining the OMI row anomaly as requested by reviewer #1
- Pg 7 Line 35 to Pg 8 Line 16: Reworded paragraph on sun glint classification to further clarify the methodology for determining sun glint affected pixels as there were some questions about this from reviewer #2

Section 3.1 Global Comparison of GLER and OMI-derived LER

- Per request from reviewer #1, we have added statistics for July 2006 to scatterplots and statistics tables to show that GLER captures the seasonality. Additionally we have added a screen on the solar zenith angle (ignore data above $70^{o}$) as high viewing angles can include cloud shadowing that decrease the OMI-derived LER.
- Added a new table to shows the statistics using the MODIS GCF per request from reviewer #1
- Corrected clerical error in Table #2 (now Table #3)
- Have made some changes to the text to address to acknowledge the additional information added to the scatterplots and statistics tables

Section 3.3 Simulating GLER with Aerosols

- Reviewer #1 noted that we only included a single orbit of data, so we have added all others orbits from April 10, 2006 into this analysis. The addition of more data had little impact on the results, but we have made note in the text that this is a specific test case as further analysis while likely be needed to formally quantify the aerosol impact on LER at these wavelengths.

Section 3.4 Inter-annual Variability of LER

- As requested by reviewer #2, we have added the wind speed, chlorophyll, and sun-glint angle to Figure 9 showing that the seasonal variability is simply caused by the seasonality in the sun glint

Section 3.5 Sensitivity to Chlorophyll and Wind Speed

- In response to a question from reviewer #1 about the method of the sensitivity test, we made minor changes to the wording of text to clarify how GLER was perturbed for the sensitivity analysis.

Appendix C Description of Look Up Tables

- We decided to include a brief paragraph in the appendix to describe the look up table approach that was used for processing GLER over the OMI mission

We greatly appreciate and thank the reviewers for their efforts related to this manuscript. They have provided important comments which have lead to several improvements in the paper. All comments from reviewers have been addressed below. *Reviewers' comments/questions below are denoted with italics,* responses are in plain text, **and additions to the manuscript are in bold**.

# Responses to Reviewer 1:

*Section 3.1: The analysis is based on data for a single month (January). It is evident form Fig. 9 that there a large seasonal variability in the lambertian-equivalent ocean surface reflectivity which is due to the changing viewing geometry as well as changes in the input parameters. It is unclear if the numbers you quote in the section are applicable to other seasons or to the whole product. I suggest either adding data for June or redoing the analysis for a yearly (sub)sample. This is especially pertinent to any use of this product as a replacement for climatological datasets.*

*p. 10, l.1: Quote: "the cloud screening methods produce similar results with only small differences that do not impact the overall evaluation." To support the above statement I suggest adding a third table showing statistics for the left column of Figure 1.*

In response to the reviewer's first comments, we have included July 2006 results in the analysis for Section 3.1 and additionally added a table to show the statistics when MODIS GCF = 0.0. The reviewer makes a good comment about this quote which has been revised to note that the Raman based ECF leads to a better comparison than the MODIS GCF.

Pg 9 lines 3-5, we made a few changes to discuss the July 2006 data:

"As shown in Table 2, the GLER and the OMI-derived LER compare best **in January** at 388 nm where $R^2$ is 0.76 and the bias is 0.002 **with the Raman ECF (using the MODIS GCF $R^2$ is 0.60 and the bias is 0.007)."**

Pg 10 lines 1-6 were changed to account for the addition of the MODIS GCF in the comparison tables and the quote the reviewer noted above was changed

**"Overall the comparison is better using the Raman ECF cloud screen than when using the MODIS GCF. This is expected given that there is a 15 minute window between the** Aqua and Aura **overpass times in 2006 (becomes 7 minutes in 2009) leading to some change in cloud cover**. It is also worth noting since OMI has a wider swath than MODIS, cloud retrievals are not available **from MODIS** for pixels on the edge of the OMI swath (these pixels are not shown in Fig. 1). **For these reasons the Raman ECF will be used for cloud screening in the rest of the paper."**

*top of the p. 11: I do not see "two main regions" in Fig.2 . It is not clear what two "distributions" the authors refer to as there is not clustering in the data. The range of*
*0.2-0.4 mentioned in the text appear to be arbitrary.*

To make this paragraph more clear we have removed this statement as it has no impact on the results.

*p. 15 Fig 8 and its analysis in the text: Figure 8 attempts to analyze the influence of aerosols based on the data from a single random orbit with a specific dependence of AOD on VZA. This analysis is obviously statistically insignificant and thus meaningless. A physical quantity like AOD should not depend on the observational geometry. Any such dependence is an indication of either a problem with the data or a lack of statistical power of the dataset. I suggest either removing this figure or redoing the analysis based on a better sample.*

The reviewer was correct that we were showing only a limited sample so we have now included all orbits for April 10, 2006 over the Pacific Ocean. The original figure showed spatial dependence in AOD which caused a crosstrack dependence of AOD with higher AOD on the west side which is close to Asia. By adding the orbits for the rest of the day over the Pacific Ocean, this issue has been resolved (see Fig 8). This analysis is simply a small case study that shows the possible impact of aerosols. A more rigorous evaluation is needed to determine the exact quantitative impact of aerosols but is outside the scope of this paper and will be investigated further in the future.

We have reworded text in section 3.3 to make it more clear that this is simply a case study to show possible aerosol effects on the GLER results.

Pg 14 lines 6-8 the following word choice changes were made:

"Figure 5 shows the **MERRA-2 AOD and the LER change for orbit 9229 where AOD ranges** from around 0.05 in the South Pacific gyre to larger than 0.4 in the northern Pacific."

Pg 15 line 6-7, we updated the 466nm slope and RMSE for additional orbits in aerosol analysis

"The combination of these changes improves the slope from **1.16** before considering aerosols **at 466 nm** to **1.0** after aerosols are introduced."

Pg 15 lines 10-11, following sentence added to note the LER difference across the swath:
**"Figure 8 shows that aerosols increase GLER generally by 0.01-0.02, with the largest increase at large forward scattering angles."**

Pg 15, line 12, stylistic change was made to remove "*on the whole*"

Pg 15, line 16-17, stylistic change was made to change "*little to no change*" to "**small decrease in LER**"

Pg 16, lines 3-8, some text was reworded to emphasize that this is simply a case study

**"In this case study**, we note that an AOD of 0.1-0.15 **increased the LER by** as much as **0.01-0.02 at 466nm, with the largest increase being** in the forward scattering direction. At 354nm, however, similar AOD values **slightly decrease LER in the backward scatter** direction, but can increase LER by as much as 0.01 in the forward scattering direction. **While this analysis was for only a specific case study, we note that the aerosol contribution likely accounts for some of the difference between GLER and the OMI-derived LER."**

*p.16, caption for Fig.9 and p.17 l. 8: Readers should not be expected to be familiar with the OMI row anomaly. Some discussion and explanation of why a specific row was used is needed*

We have added the following text to section 2.6, pg 7, lines 14-20:

**"Beginning in mid-2007, OMI experienced an anomaly known as the "row anomaly" that has affected the L1b radiance data. There have been several impacts from the row anomaly including decreased radiances due to possible blockage, increased signal due sunlight being reflected into the instrument, a wavelength shift due to a change in the slit function, and earthshine radiances from outside the FOV that are reflected into the nadir port. The row anomaly is further explained in Schenkeveld et al. (2017). For this reason, after 2007 we focus only on rows 1-21, which are not affected by the row anomaly."**

*p.17, l. 14: Quote: " in Fig. 10 there is a small downward trend in the difference between GLER and OMI-derived LER of at most 0.005 LER. This may be related to the downward drift in the OMI measurements" While it may be correct, the authors do not present enough evidence to support the statement and do not consider other possibilities. Trends in the auxiliary may be responsible. The authors used wind datasets from two different instruments with the switch occurring in the middle of the data series. How do the two datasets compare and could the switch affect the trend? In order to support their statement the author could adjust the calculations for the downward drift in the OMI measurements and see if they can reproduce the trend.*

The reviewer raises an important point about other possible causes for the trend in the LER difference. We do note, however, that if the cause of the drift was the wind speed, the largest change would be at the longer wavelengths where the direct reflectance is more important and wind speed uncertainty is the greatest as shown in section 3.5.

Additionally, reviewer #2 has requested the inclusion of sun-glint angle, wind speed, and chlorophyll in Fig. 9. The change as noted in 2011 in the wind speeds is quite small and there is no apparent drift after this point. From 2016-2018, both

wind speed and chlorophyll appear quite consistent, but the GLER-OMI difference still appears to drift through these 3 years.

Attached we have included Fig 1. of the response in which we took Fig. 9 and de-seasonalized the data in order to better see the trends. As seen in Fig. 10, the trend in the LER difference at 354nm is only 0.005 and negligible at 466nm. Based on Fig. 1 of the response, at 354nm it appears that while GLER seems consistent, OMI LER does decrease starting around 2011/2012. We do note, there are some year to year changes in LER possibly due to phenomenon such as El Nino/La Nina, but such changes are captured both by GLER and OMI-derived LER.

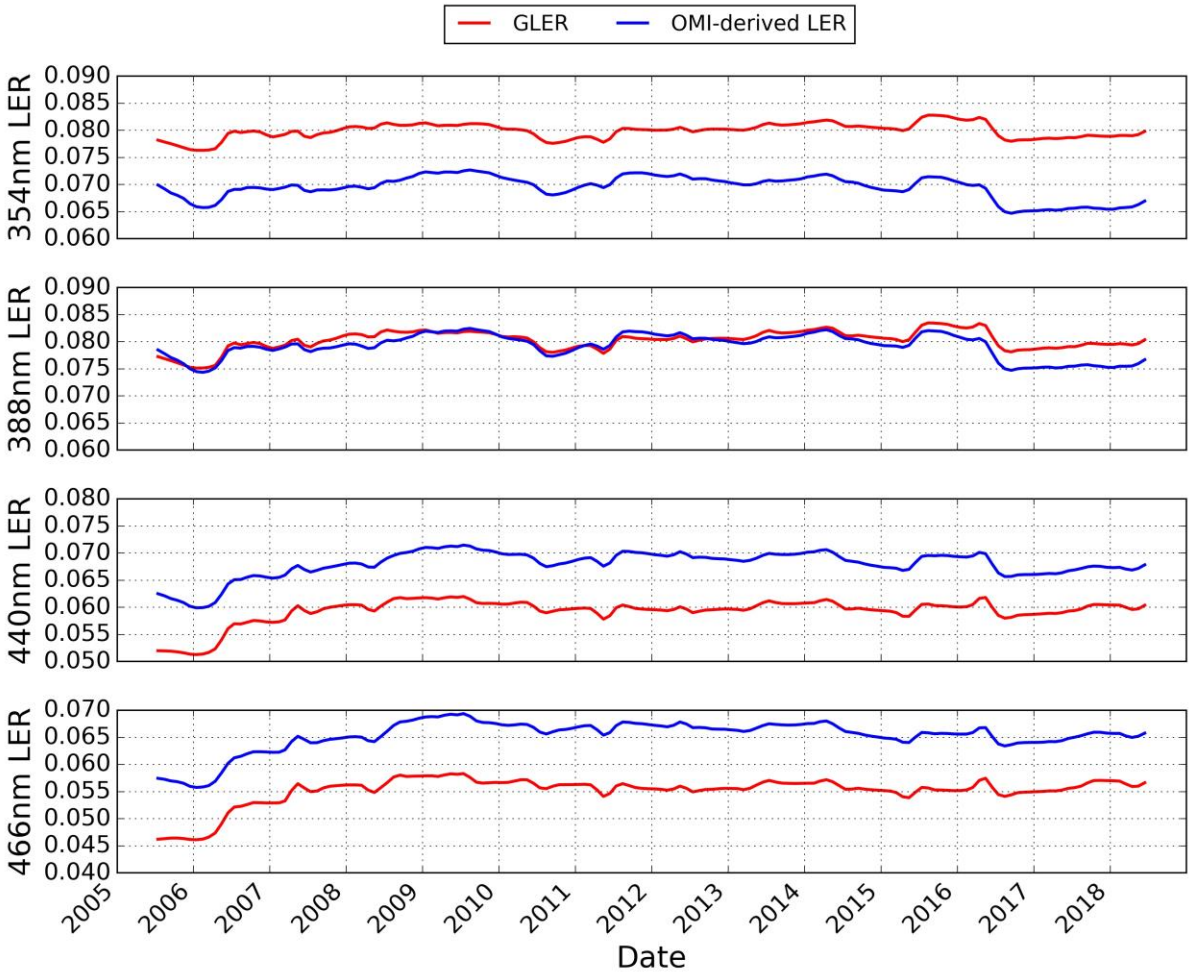


Figure 1: De-seasonalized trend of GLER and OMI LER corresponding to Fig. 9 of the original manuscript. All data were screened the same as Fig. 9.

The general consensus is that the OMI drift is 1-1.5% radiance through the first 10 years of the OMI mission as noted by Schenkeveld et al. 2017. We see a drift of about 0.005 in LER at 354nm, which corresponds to around a 1% drift through the

OMI mission. The OMI team is currently working to assess the drift and will be applying a correction to the radiance data in the next version of L1b processing.

Pg 16 lines 23-26 were changed to be more precise about the current accepted rate of the OMI drift:

"We note that in Fig. 10 there is a small downward trend in the difference between GLER and OMI-derived LER of at most 0.005 in LER. **At 354nm a change of 0.005 LER corresponds to approximately 1% in TOA radiance which is close to the 1-1.5% TOA radiance degradation noted by Schenkeveld et al. 2017."**

*p.18 l.22 Wind speed and chlorophyll are two independent variables. Please describe how they were jointly perturbed to produce the results in Table 5.*

We re-calculated GLER by perturbing the wind speed and chlorophyll in either direction by their assumed uncertainty. In the case of the combined perturbations, we simply perturbed each input in 4 possible directions (CHL high & WSP high; CHL low & WSP low; CHL high & WSP low; CHL low & WHP high) and then simply averaged the magnitude of the difference between the original LER and the adjusted LER. Additionally, we determined the maximum LER difference from all possible scenarios.

Pg 19 Lines 14-19 were changed (updated text in bold) to address this concern:

**"To determine the combined effect, we additionally calculated GLER perturbing both the wind speed and chlorophyll for the four possible combinations.** Table 6 shows the mean difference **from the combined sensitivity analysis** in GLER is similar to that obtained **by only perturbing the chlorophyll**. The maximum difference from the combined sensitivity test, however, is similar to that of the wind speed perturbation. This is because while the wind speed has a significant impact on sun glint, only a small fraction of OMI pixels are impacted by glint."

Technical corrections
*p.2, l. 5: due to*

*p.2, l. 12: "angle" is missing after viewing*

*p.8 Section 3.1 tables and graphs: The correspondence between tables and plots is not clear. Please state that*
*Table 1 provides statistics for right column plots of Fig.1 in the caption. Same for Table*
*2 p.9, Fig. 1 caption's last sentence : Clarify that the left and right columns are for two*
*cloud screening methods.*

*p.20, l. 17: "combination of things" does not sound good;*
*effects or factors?*

We greatly appreciate the reviewer noting these corrections and have made the corrections in the manuscript.

# Responses to Reviewer 2:

*Page 7, line 34-35 reads "We select sun glint scenes when the difference between the measured LER at 354 nm and 388 nm is less than -0.05." How is the threshold value chosen? Is there any reference or evidences indicating this number represents a good threshold? And why not define sun glint based on the sun-glint angle (or sun-glint angle)?*

We changed the terminology of co-scattering angle to sun-glint angle because ultimately that is all that we meant by the co-scattering angle. Since sun-glint angle is more well known, we have taken the reviewers advice in making the change.

The reviewer raises some good questions about the methodology for choosing sun glint scenes. There appears to be some confusion with the text in the explanation of the sun glint scenes. We first focus on scenes where the sun-glint angle is less than 20 degrees and then additionally apply the LER difference screen. The reason for the LER difference screen is that clouds in the sun glint region are difficult to detect and therefore remove. Cloud fractions are typically biased high for sun glint regions making separation between clouds and sun glint challenging. By using the LER difference screen, we are able to more easily distinguish between clouds and sun glint.

Pg 7 Line 30-Pg 8 Line 4 was updated to address this concern:

"We compare cases with and without sun glint separately because the reflection of light in each case is quite different. For comparisons excluding sun glint scenes, we screen out data with a sun-glint angle of less than $20^o$ in which sun glint can occur. For the comparisons with sun glint, **while the sun-glint angle of $20^o$ is again used to choose the sun glint region, additional screening based on the spectral dependence of the measured LER is performed to remove clouds within the sun glint region. The reason for this is that cloud fraction retrievals are affected by sun glint. The** difference in LER occurs because of a spectrally dependent error in the underestimation of the Rayleigh scattering of diffuse light when one assumes a Lambertian ocean surface, when the reflectance is in fact specular. We select sun glint scenes when the difference between the measured LER at 354 nm and 388 nm is less than -0.05**. We note that some weaker sun glint has an LER difference that is not below this threshold, but here we focus on stronger glint that has no cloud contamination."**

We do note that due to a clerical error, a few values in Table 2 were incorrect, but this has since been corrected. The change is minor and does not have any impact on the final conclusions of the paper.

We did put some more thought to the threshold that was used for the LER difference in response to the reviewer's questions about it. We have done this by comparing the LER difference (354nm-388nm) from the OMI measurements with the absolute LER at 466nm from OMI. This analysis shown in Fig. 1 of the response shows two different distributions of data for cloud and sun glint. The data affected by clouds have a slope of nearly 0, whereas the sun glint data show a strong negative slope since the error in LER for sun glint is spectrally dependent. Using this shows that a threshold of -0.05 distinguishes sun glint from clouds. Below is the figure showing this comparison for January 2006 for data with a sun-glint angle less than $20^{o}$. The cutoff of -0.05 is shown in the solid black line with everything below it being included in the sun glint analysis.

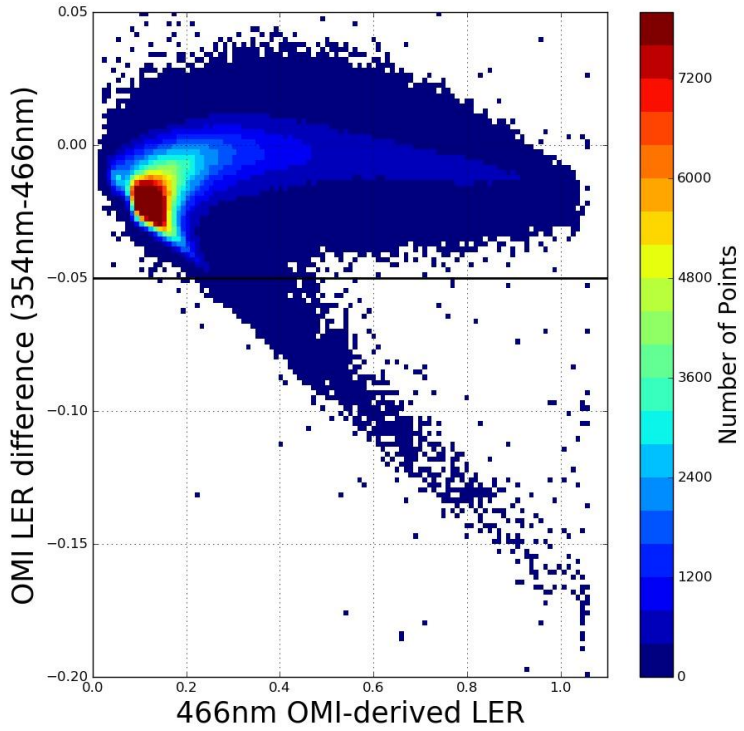


Figure 1: Comparison of 466nm OMI-derived LER and the difference between 354nm and 466nm OMI-derived LER for January 2006.

Similarly in Fig. 2 of the response, we plotted the LER difference as a function of crosstrack position for January 2006 for sun-glint angles less than 20$^{o}$. For OMI, sun glint typically occurs in rows 10-30. Here it also appears clear that a cutoff of -0.05 is effective to define the strong sun glint region.

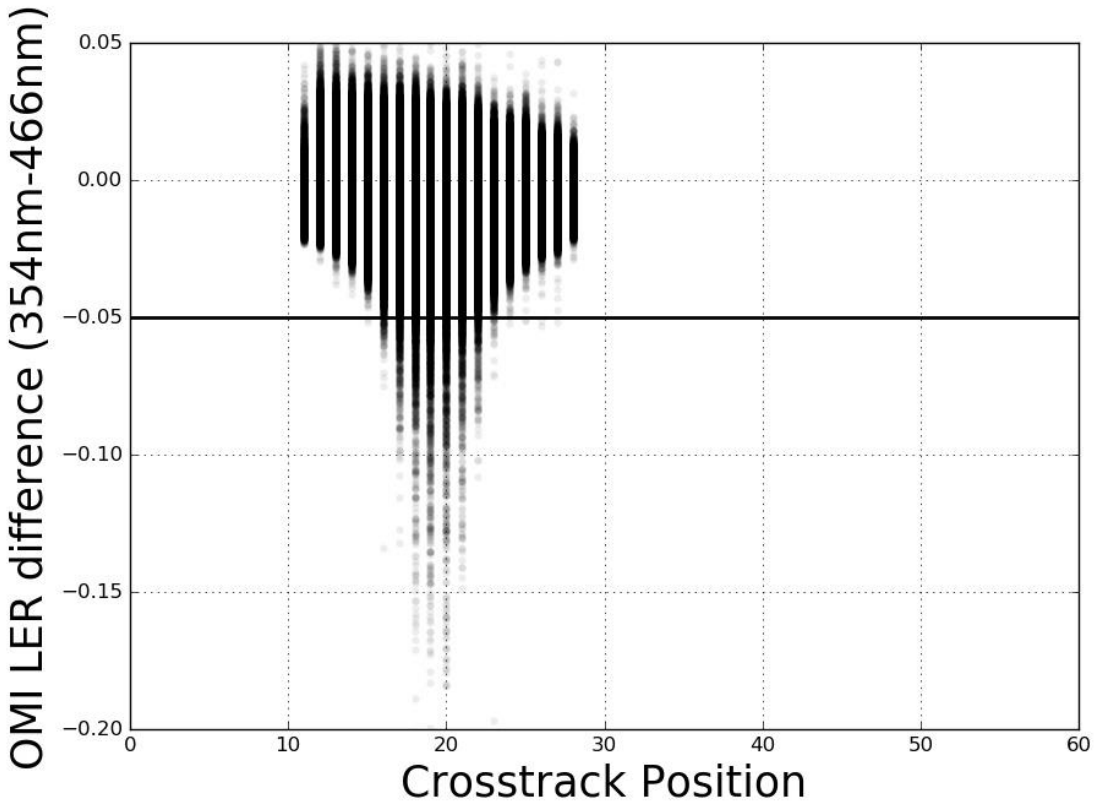


Fig 2: LER difference plotted as a function of crosstrack for sun glint possible pixels defined as sun-glint angle less than 20 degrees

Finally, Fig. 3 of the response compares MODIS visible satellite imagery with OMI LER at 466nm and the LER difference from OMI to show that a threshold of -0.05 does a good job defining the stronger glint region.

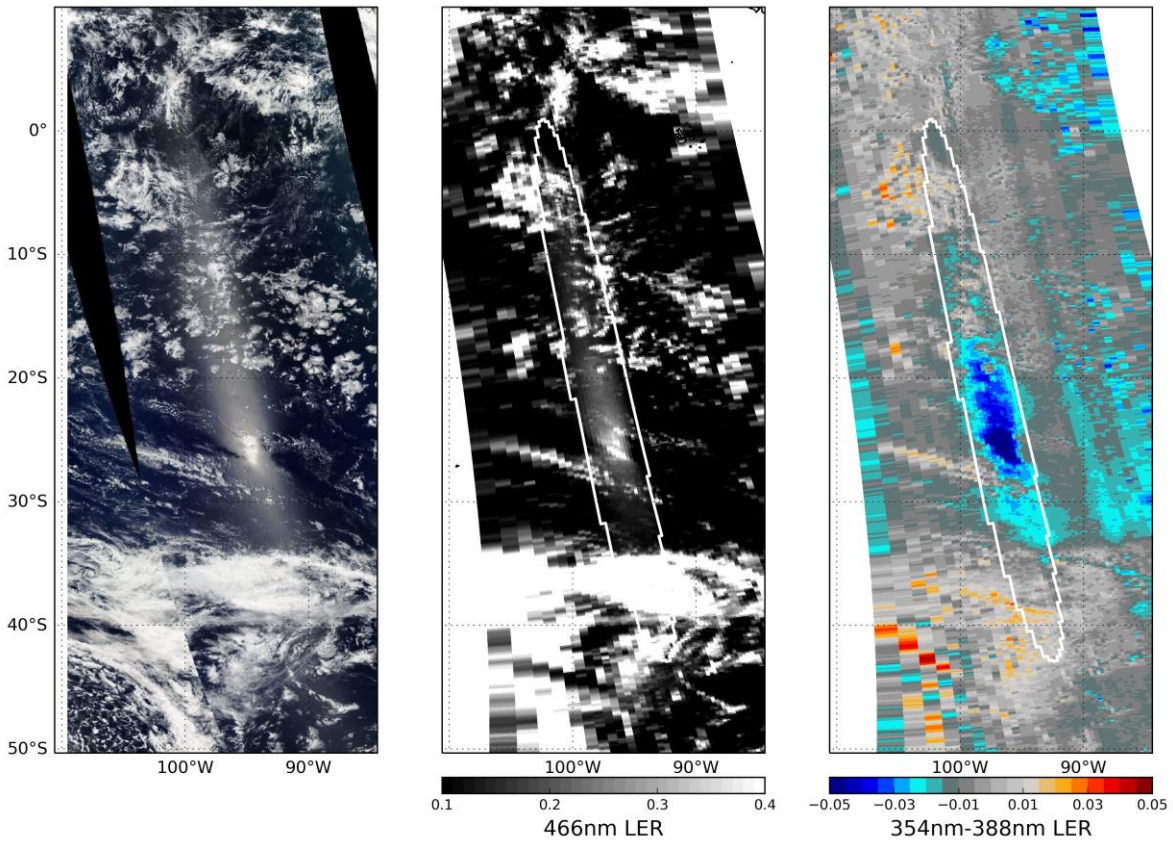


Figure 3: OMI Delta R for an orbit on Jan 3, 2006 compared with the 466nm OMI-derived LER in the middle and MODIS visible satellite imagery on left

We note that this threshold is arbitrary in how it is chosen, but we feel that this provides the best evaluation of the sun glint data in avoiding contamination from clouds. We have refrained from including these figures in the paper at this time since the focus of this paper is not on the evaluation of our sun glint model.

*Page 17, line 3-5: "There is also a seasonal variation in GLER due to the changing viewing geometry of satellite measurements as the SZA changes through the year." Can the authors add more evidence to prove this statement? It seems to the sun glint may play an import role in the seasonal variation. I also curious if the seasonal variation is also related to any seasonal changes in wind speed or chlorophyl concentration. So it would be helpful if the time series for, sun glint angle, wind speed, and chlorophyll concentration are also provided (at least examined by the authors).*
*Ok. Continuing my last comment, the sensitivity analysis in section 3.5 indeed confirms that changes in chlorophyll concentration will not be able to cause the GLER seasonal variation.*

Per the reviewers' request, we have added these additional data to Fig. 9 and show that the seasonality is mainly due to the sun-glint angle seasonality. This request is very beneficial as it also addresses a question by reviewer 1 asking whether the chlorophyll or wind speed measurements could cause the drift in the GLER – OMI-derived LER difference. This figure shows that there is not a similar drift in either of the measurements meaning that the drift in the differences is likely at least partly instrumental.

*Page 22, line 18: "lambda" is . –> "lambda" is the wavelength.*

We have made the change noted by the reviewer.

Manuscript prepared for Atmos. Meas. Tech.
with version 3.0 of the LaTeX class copernicus.cls.
Date: 14 October 2019

# A geometry-dependent surface Lambertian-equivalent reflectivity product for UV/Vis retrievals: Part ~~II.~~ 2: Evaluation over open ocean

Zachary Fasnacht[1], Alexander Vasilkov[1], David Haffner[1], Wenhan Qin[1], Joanna Joiner[2], Nickolay Krotkov[2], Andrew M. Sayer[3], and Robert Spurr[4]

[1]Science Systems and Applications Inc., Lanham, MD, USA
[2]NASA Goddard Space Flight Center, Greenbelt, MD, USA
[3]GESTAR, Universities Space Research Association, Columbia, MD, USA
[4]RT Solutions Inc., Cambridge, MA, USA

*Correspondence to:* Z. Fasnacht (zachary.fasnacht@ssaihq.com)

**Abstract.** Satellite-based cloud, aerosol, and trace gas retrievals from ultraviolet (UV) and visible (Vis) wavelengths depend on the accurate representation of surface reflectivity. Current UV and Vis retrieval algorithms typically use surface reflectivity climatologies that do not account for variation in satellite viewing geometry or surface roughness. The concept of geometry-dependent surface Lambertian-equivalent reflectivity (GLER) is implemented for water surfaces to account for surface anisotropy using a Case 1 water optical model and the Cox-Munk slope distribution for ocean surface roughness. GLER is compared with Lambertian-Equivalent reflectivity (LER) derived from the Ozone Monitoring Instrument (OMI) for clear scenes at 354, 388, 440, and 466 nm. We show that GLER compares well with the measured LER data over the open ocean and captures the directionality effects not accounted for in climatological LER databases. Small biases are seen when GLER and the OMI-derived LER are compared. GLER is biased low by up to 0.01-0.02 at Vis wavelengths, and biased high by around 0.01 in the UV, particularly at 354 nm. Our evaluation shows that GLER is an improvement upon climatological LER databases as it compares well with OMI measurements, and captures the directionality effects of surface reflectance.

## 1 Introduction

Satellite retrievals of clouds, aerosols, and trace gases rely on the accurate representation of surface reflectivity. Many modern satellite ultraviolet (UV) and visible (Vis) trace gas algorithms use the mixed ~~Lambert equivalent~~ Lambertian-equivalent reflectivity (LER) model which assumes the measured top-of-atmosphere (TOA) radiance is a combination of the clear and cloudy sky radiances

weighted by an effective cloud fraction (ECF) (Koelemeijer et al., 2001; Seftor et al., 1994; Stammes et al., 2008). While many databases of LER currently exist, they are typically climatological LER ~~data sets~~ datasets based on the minimum or the mode of the LER distribution. Therefore, they do not account for the directionality effects due to the variation of satellite viewing and solar illumination geometries. Further, they do not capture day to day change in the roughness of the water surface due to changing wind speed which can impact surface reflectance. Additionally, climatological LER databases may be affected by residual aerosol and cloud contamination. These databases include Kleipool et al. (2008) using data from the Ozone Monitoring Instrument (OMI) for wavelengths 328-499 nm, Koelemeijer et al. (2003) from the Global Ozone Monitoring Experiment (GOME) for wavelengths 335-772 nm, and Tilstra et al. (2017) from GOME-2 for wavelengths between 335-772 nm.

The bidirectional reflectance distribution function (BRDF) describes the ~~reflectivity of a surface~~ variations of the surface reflectivity for all illumination and viewing geometries. Given a specific solar and viewing angle from a satellite and the BRDF of the surface, a quantity known as the bidirectional reflectance factor (BRF) can be derived for that surface. BRF is defined as the ratio of the radiant flux reflected by a surface to the radiant flux reflected into the identical beam geometry by an ideal diffuse Lambertian surface, irradiated under the same conditions as the sample surface (Schaepman-Strub et al., 2006). A peak in the BRDF arises due to sun glint phenomena when the ~~the~~ sun and satellite viewing angles are similar and oriented in a forward scattering geometry. Sun glint is strongest for smooth water surfaces that permit nearly perfect Fresnel reflection of direct light from the ocean surface (Kay et al., 2009; Cox and Munk, 1954; Thomas et al., 2012). ~~Another feature of the BRDF over water occurs~~ Additionally, there is an increase in radiance near the outer edges of the satellite swath viewing geometry, when TOA radiances increase due to increased effects of Rayleigh scattering. The increase in diffuse sky reflection from the ocean surface becomes more significant at these longer path lengths, and the relative contributions from the water leaving radiance to the intensity reaching the satellite is reduced (Vasilkov et al., 2017).

Vasilkov et al. (2017) introduced a concept known as geometry-dependent LER (GLER), where for a specific viewing geometry, TOA radiances are simulated over a non-Lambertian surface using the BRDF. GLER can be easily implemented into trace gas algorithms by simply replacing the currently used LER climatologies. For Vis wavelengths, the change in surface reflectivity associated with implementation of GLER was found to directly decrease the OMI $NO_2$ air mass factor (AMF) over land and oceans by as much as 15%, and change the OMI $NO_2$ AMF indirectly by an additional $-22\%$ to 13% through changes to retrieved cloud properties (Vasilkov et al., 2017). In the UV, Ahn et al. (2014) noted that unrealistic surface albedo is one of the main causes for uncertainty in aerosol retrievals, while Torres et al. (1998) reported that surface albedo errors can lead to as much as a 5% error in retrieved aerosol optical depth (AOD) for weakly absorbing aerosols. ~~? showed that for clear scenes, errors in surface reflectivity in the UV can lead to as much as an 8% error in the calculation~~

~~of AMF over oceans.~~

Qin et al. (2019) evaluated the OMI 466 nm GLER product over land generated using BRDF data from the Moderate Resolution Imaging Spectroradiometer (MODIS). They compared GLER with OMI-derived LER globally and found GLER was biased low by 0.01 to 0.02 relative to OMI. The difference was attributed to several factors, including small calibration differences between MODIS and OMI and possible residual cloud and/or aerosol contamination in the OMI data that was not completely filtered out.

Here we evaluate the GLER product generated for the OMI instrument for ocean scenes. OMI is a hyperspectral UV-Vis (270-500 nm) imager onboard the NASA Aura satellite, which was launched in July 2004. The high spectral resolution (0.42-0.63 nm) of the UV (270-370 nm) and Vis (350-500 nm) channels enables retrievals of many important atmospheric constituents including $O_3$, $NO_2$, $SO_2$, and aerosols. OMI has a spatial resolution of 13 km x 24 km at nadir with a field of view (FOV) of 0.8° in the flight direction and 115° across the swath. Prior to 2008, OMI provided global coverage daily with a repeat cycle of 16 days. The OMI row anomaly affects data coverage starting in mid-2007 (Schenkeveld et al., 2017), but a substantial amount of high quality global data remain available thereafter.

In this work we focus on evaluation of GLER at UV and Vis wavelengths over oceans. In the UV, 354 nm and 388 nm are chosen for evaluation as both ~~have importance~~ are important in the OMI retrieval of aerosol properties (Torres et al., 2007) and additionally OMI Raman cloud retrievals are performed at 354 nm (Vasilkov et al., 2008). For Vis wavelengths, 440 nm and 466 nm are chosen as they are important for $O_2$-$O_2$ cloud retrievals (Vasilkov et al., 2017; Veefkind et al., 2016) as well as $NO_2$ retrievals (Krotkov et al., 2017; Lamsal et al., 2014).

Whereas the land product described in Qin et al. (2019) used a model of BRDF with input from MODIS, GLER for ocean scenes is produced solely by modeling of water-leaving radiance and surface reflection. These surface-leaving radiance contributions are geometry-dependent, and the anisotropic nature of light backscattered by the ocean has been studied in many papers (see e.g., Gordon (1989); Morel and Gentili (1991, 1993, 1996); Park and Ruddick (2005); Lee et al. (2013)). For GLER, water-leaving radiance is simulated using a Case 1 water model (Morel, 1988; Morel and Maritorena, 2001) that depends only on chlorophyll concentration. This model is described in detail in Sect. 2.2. Reflection from the ocean surface is modeled using the Cox-Munk slope distribution (Cox and Munk, 1954) and is further described in Sect. 2.3.

The algorithms and approaches described in this paper are relevant to NASA's future Plankton, Aerosol, Cloud, ocean Ecosystem ~~mission~~ (PACE) mission. PACE is currently ~~is~~ planned to launch in 2022-2023. Global PACE observations will provide data to monitor oceanic and atmospheric variables important for Earth ecosystem, carbon cycle, and climate studies. The PACE Ocean Color Instrument (OCI) is designed as a wide-swath imaging spectrometer with a 1 km ground nadir resolution, a 5 nm spectral resolution between 345 and 890 nm and several short wave infrared bands

(Werdell et al., 2019). As compared with the Sea-Viewing Wide Field-of-View Sensor (SeaWiFS), the MODerate resolution Imaging Spectrometer (MODIS), and the Visible Infrared Imaging Radiometer Suite (VIIRS), the OCI will additionally measure TOA radiances in the UV to help identify phytoplankton composition and harmful algal blooms. PACE's spectral coverage from UV-A to green wavelength region and in the red-NIR will enable unparalleled evaluation of ocean ecosystem properties in optically complex waters and in regions of increasing eutrophication (Cetinic et al., 2018).

## 2 Data and Methods

### 2.1 VLIDORT Radiative Transfer Model

For radiative transfer calculations we use the Vector Linearized Discrete Ordinate Radiative Transfer (VLIDORT) model. VLIDORT is a multiple scattering radiative transfer model that can simulate Stokes vectors at any level in the atmosphere and for any scattering geometry with a Lambertian or non-Lambertian underlying surface (Spurr, 2006; Spurr et al., 2019). VLIDORT can simulate attenuation of solar and line-of-sight ~~paths~~ path radiances in a spherical atmosphere. In this study, we correct for the effects of atmospheric sphericity for both incoming solar and outgoing viewing directions based on a regular pseudo-spherical geometry calculation. This is important for large solar and viewing zenith angles. We also include polarization using the vector mode, because to neglect it can lead to considerable errors for modeling backscattered radiances in the UV/Vis wavelength range.

### 2.2 Water-Leaving Radiance Implementation

VLIDORT has a supplement ("VSLEAVE") for the generation of surface-leaving radiances for use as inputs to the main radiative transfer calculation in the atmosphere. This supplement can be used for either simulations of solar-induced fluorescence or water-leaving radiances from Case 1 waters. Our Case 1 water model accounts for the bi-directional effects following Morel and Gentili (1996). In this paper we do not account for vibrational-Raman scattering in ocean water (Morel et al., 2002; Vasilkov et al., 2002). The common Case 1 water model developed for the Vis (Morel, 1988) was extended to the UV using a parameterization of the particulate matter absorption coefficient from Vasilkov et al. (2002, 2005). The model requires as input several quantities that affect absorption and scattering properties of sea-water and its constituents. Extinction coefficients for water absorption are taken from Lee et al. (2015), chlorophyll absorption coefficients from Vasilkov et al. (2005) below 400 nm and Lee et al. (2005) at longer wavelengths, and CDOM absorption from Morel and Maritorena (2001). The water scattering coefficients we use are from Morel et al. (2007) and for chlorophyll scattering, Morel and Maritorena (2001). A detailed description of these parameteriza-

tions is provided in Appendix A2.

The computation of emerging water-leaving radiance $L_w$ depends not only on the optical properties of marine constituents and radiative processes in the near-surface ocean, but also on the total atmospheric direct and diffuse downwelling transmittance $T_{atm}$ of atmospheric light through the air-water interface. This complicates separation of the water-leaving calculation and the calculation of atmospheric radiance propagation~~in the atmosphere~~. Additionally, $T_{atm}$ will in general depend on the surface leaving contribution and hence on marine constituents. VLIDORT and its supplement VSLEAVE are therefore coupled. This coupling can be treated formally with a coupled ocean-atmosphere radiative transfer model such as that described in Spurr et al. (2007). Here, however, we have developed a simple coupling scheme for VLIDORT that ensures the value of $L_w$ used as a input at the ocean surface will correspond to the correct value of the downwelling flux reaching the surface interface. The first applications of this new water-leaving model were presented in Vasilkov et al. (2017) and Sayer et al. (2017). The coupled model approach is described further in Appendix B.

### 2.3 Cox-Munk BRDF Implementation

A supplement ("VBRDF") is implemented in VLIDORT to account for the reflection of the water surface using the Cox-Munk slope distribution (Cox and Munk, 1954). We use the full form of the Cox-Munk distribution in which the facet slope variance depends on both wind speed and wind direction. Polarization at the ocean surface is accounted for using a full Fresnel reflection matrix as suggested by Mishchenko and Travis (1997). Additionally we account for contributions from oceanic foam that can be significant for high wind speeds using work by Frouin et al. (1996).

### 2.4 Ancillary Data for Water Model

As mentioned in the introduction, modeling of the water leaving radiance requires information on the chlorophyll concentration and the modeling of Cox-Munk surface roughness depends on wind speed and wind direction. These inputs are not available directly from the OMI satellite and so other sources of ancillary inputs are required.

The wind speed measurements for GLER come from a pair of satellite microwave imagers. ~~Wind speed data are from~~ The first is the Advanced Microwave Scanning Radiometer - Earth Observing System (AMSR-E) instrument onboard the NASA Aqua satellite with a spatial resolution of 0.25° (Wentz and Meissner, 2004). The ~~AMSRE-E~~ AMSR-E instrument, however, ceased operations in October 2011 due to an issue with the spinning mechanism (Wentz and Meissner, 2007). After October 2011, data are taken from the Special Microwave Imager/Sounder (SSMIS) with a spatial resolution of 0.25°. SSMIS is onboard the Air Force Defense Meteorological Satellite Program

(DMSP) Satellite F16 (Wentz, et al., 2012). While the SSMIS instrument has been operating since October 2003, the AMSR-E instrument was chosen for the first half of the OMI mission due to the small difference in equator crossing times of 7-15 minutes between the Aqua and Aura satellites, wheres the F16 satellite crossing times range from 6 hours behind Aura in 2005 to 2 hours behind Aura currently. In future work, we plan to replace the SSMIS F16 wind speed with the AMSR-2 wind speed data. AMSR-2 is on board the Global Change Observation Mission Water Satellite 1 (GCOM-W1) which has an equator crossing time more similar to OMI (Imaoka et al., 2012). Gaps in the wind speed data due to extreme glint or rain are filled by the Global Modeling Assimilation Office (GMAO) Goddard Earth Observing System Model Forward Processing for Instrument Teams (GEOS-5 FP-IT) near real-time assimilation with a spatial resolution of 0.625° longitude by 0.5° latitude and a temporal resolution of 3 hours (Lucchesi, 2013). Wind direction data are also from the GEOS-5 FP-IT model.

Monthly chlorophyll data from the MODIS instrument~~which is on board~~, which is onboard NASA Aqua satellite, were used in modeling of the water leaving radiance (Hu et al., 2012). These chlorophyll data have a spatial resolution of 4 km. The MODIS daily chlorophyll data are not used due to large gaps caused by clouds and aerosols. Some gaps still exist in the monthly data and are filled by other ~~data sets~~ datasets from the MODIS team. These include ~~a~~ monthly climatological and yearly chlorophyll ~~data set~~ datasets which are also at a 4 km resolution. The benefit of using the monthly chlorophyll data instead of the climatological data comes from the ability to capture inter-annual trends due to phenomena such as the El Niño-Southern Oscillation (ENSO).

### 2.5 Calculation of LER and GLER

Using the equation from Dave (1978), LER ($R$) can be calculated from TOA Radiance ($I_{comp}$) by inverting the following:

$$I_{\mathrm{comp}}(\lambda,\theta,\theta_0,\phi,P_s,\mathrm{BRF}_s) \approx I_0(\lambda,\theta,\theta_0,\phi,P_s) + \frac{RT(\lambda,\theta,\theta_0,P_s)}{1-RS_b(\lambda,P_s)}, \quad (1)$$

where $\lambda$ is wavelength, $\theta$ is the viewing zenith angle (VZA), $\theta_0$ the solar zenith angle (SZA), $\phi$ the relative azimuth angle (RAA), $P_s$ is the surface pressure, $I_0$ is the path scattering radiance by the atmosphere, calculated as the TOA radiance for a black surface, $T$ is total (direct+diffuse) solar irradiance reaching surface and reflected back the satellite multiplied by the transmittance, $S_b$ is the diffuse flux reflectivity of the atmosphere, and R is LER.

In order to calculate GLER, we use VLIDORT to simulate $I_{comp}$ for a clear sky over a non-Lambertian surface with the water leaving radiance model described in Sect. 2.2 along with the Cox-Munk slope distribution for surface roughness. A look-up table (LUT) approach is used to calculate TOA radiance operationally, as running VLIDORT can be computationally expensive. Details on the LUT ~~used are available in AppendixB of Qin et al. (2019)~~approach can be found in Appendix C.

Given TOA Radiance from VLIDORT, we can then calculate GLER using ~~Eqn. 1~~Eq. ( 1).

### 2.6 OMI Data and Selection Criteria

The measured LER data used to evaluate ocean GLER in this study were retrieved from OMI collection 3 level 1b Vis channel radiance data by inverting ~~Eqn. 1~~ Eq. ( 1) where $I_{obs}$ is used in place of $I_{comp}$. The OMI radiances are normalized using the OMI day-1 solar irradiance spectrum adjusted for variation in Earth-Sun distance when radiance measurements were collected. The GLER product is designed to characterize the magnitude and the angular variability of the Earth's surface reflectance in a Rayleigh atmosphere, and therefore several aspects of instrument calibration must be considered. Absolute radiometric calibration error will introduce bias and inconsistency across the measurement swath for LER at any single wavelength. Dobber et al. (2008) estimated that the uncertainty in radiometric calibration of OMI collection 3 sun-normalized radiances is under 2% and that the relative viewing angle dependence is also less than 2%. Schenkeveld et al. (2017) evaluated long-term changes in the absolute radiometric response of the OMI instrument and estimated degradation of approximately 1-1.5% ~~over the lifetime of the mission~~ per decade in the wavelength region used in this study. Since we compare results at 354, 388, 440, and 466 nm in this study, the spectral dependence of OMI calibration is also an important consideration. Little work has been published on this topic, although the study by Jaross and Warner (2008) compared the OMI sun-normalized radiances to radiative transfer model simulations over Antarctic ice, and showed that the spectral dependence of the OMI calibration is within the ~~uncertainty of the~~ absolute radiometric uncertainty.

Beginning in mid-2007, OMI experienced an anomaly known as the 'row anomaly' that has affected the L1b radiance data. There have been several impacts from the row anomaly including decreased radiances due to possible blockage, increased signal due to sunlight being reflected into the instrument, a wavelength shift due to a change in the slit function, and earthshine radiances from outside the FOV that are reflected into the nadir port. The row anomaly is further explained in Schenkeveld et al. 2017. For this reason, after 2007 we focus only on rows 1-21, which are not affected by the row anomaly.

Absorption by $O_2$-$O_2$ and $O_3$ were accounted for at 440 nm and 466 nm, but neglected for 354 nm and 388 nm. Since GLERs were simulated for a Rayleigh-only atmosphere, pixels with absorbing aerosols are removed using the OMAERUV absorbing aerosol index AI ($|AI| > 0.5$ are removed) (Torres et al., 2007). We compare the evaluation for two independent cloud screening methods to determine which will better represent the GLER evaluation. The MODIS geometrical cloud fraction (GCF) is retrieved from the 15 $\mu$m $CO_2$ absorption region (Menzel et al., 2007) and is colocated to the OMI FOV in the OMMYDCLD product (Joiner, 2014). The OMI Raman cloud product contains an ECF and cloud pressure based on rotational-Raman scattering ~~in the UV wavelengths~~ at 354 nm using the Cox-Munk distribution to model ocean surface reflectivity (Vasilkov et al., 2008).

We compare cases with and without sun glint separately because the reflection of light in each case is quite different. For comparisons excluding sun glint scenes, we screen out data with a ~~co-scattering~~ sun-glint angle of less than 20° in which sun glint can occur. For the comparisons with sun glint, ~~the data are identified by evaluating the difference between OMI measured LER at 354 and 388 . The~~ while the sun-glint angle of 20° is again used to choose the sun glint region, additional screening based on the spectral dependence of the measured LER is performed to remove clouds within the sun glint region. The reason for this is that cloud fraction retrievals are affected by sun glint. The difference in LER occurs because of a spectrally dependent error in the underestimation of the Rayleigh scattering of diffuse light when one assumes a Lambertian ocean surface, when the reflectance is in fact specular. We select sun glint scenes when the difference between the measured LER at 354 nm and 388 nm is less than -0.05. ~~This method does not require additional cloud screening, as the spectral dependence of clouds is quite small~~We note that some weaker sun glint has an LER difference that is not below this threshold, but here we focus on stronger glint that has no cloud contamination.

In addition to the OMI-derived LER, we compare with the Kleipool LER climatology (Kleipool et al., 2008), since a number of current operational algorithms use this LER data as input. There are two LER datasets available from the Kleipool data, one representing the monthly minimum LER and another determined through interpretation of LER histograms. Both are shown in our evaluation as each is used in some algorithms.

## 3 Results and Discussion

### 3.1 Global Comparison of GLER and OMI-derived LER

Table 1: Statistical analysis of GLER vs OMI LER for non-sun glint scenes
January (July) 2006 deep ocean only with raman based ECF = 0.0 (~~number~~ corresponds to 2nd and 4th columns of ~~points = 341,629~~Fig. 1)

| Wavelength | Slope | $R^2$ | Mean Bias | RMSE | Npts |
|---|---|---|---|---|---|
| 354 nm | ~~0.61~~0.63 (0.62) | ~~0.54~~ 0.57 (0.41) | -0.01 (-0.015) | ~~0.015~~0.014 (0.018) | 334,517 (111,260) |
| 388 nm | ~~0.80~~ 0.83 (0.85) | ~~0.74~~ 0.76 (0.70) | 0.002 (-0.003) | 0.008 (0.008) | 334,517 (111,260) |
| 440 nm | ~~0.76~~ 0.80 (0.72) | ~~0.69~~ 0.71 (0.65) | 0.012 (0.006) | 0.015 (0.011) | 334,517 (111,260) |
| 466 nm | ~~0.76~~ 0.82 (0.73) | ~~0.66~~ 0.68 (0.64) | 0.013 (0.01) | 0.015 (0.011) | 334,517 (111,260) |

First we compare GLER with the OMI-derived LER globally for January and July of 2006 at 4 wavelengths in Figs. 1 and 2. To determine a cloud screening method for the evaluation of sun glint free data, in Fig. 1 we compare GLER with the OMI-derived LER using the cloud screening

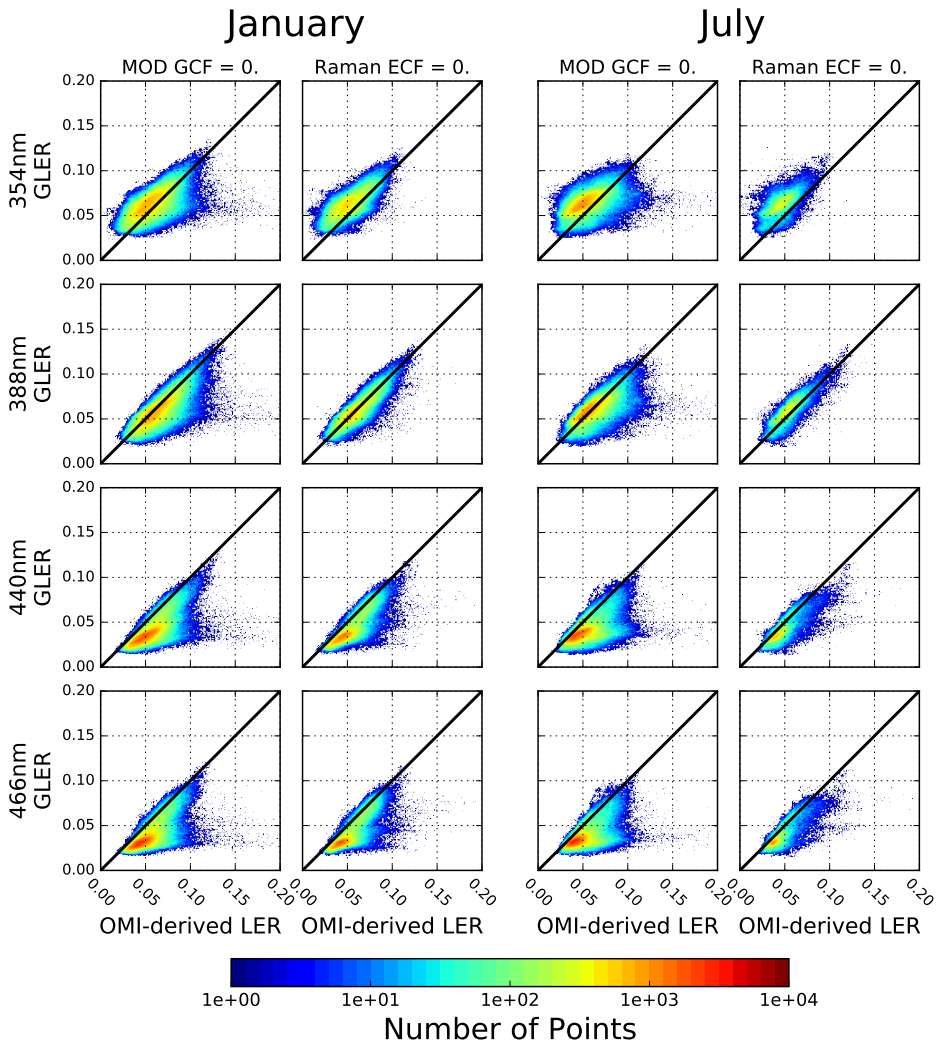


Fig. 1: Scatterplots of OMI-derived LER vs GLER for ~~January~~ two months in 2006 (January on left and July on right) with possible sun glint removed at 4 wavelengths (354 nm, 388 nm, 440 nm, and 466 nm). Data are for deep ocean (based on OMI level 1b ground pixel quality flags) and have been screened for aerosols (OMAERUV $|\mathrm{AI}| < 0.5$). Clouds are screened through two different methods which are described in Sect. 2.6. Only data with solar zenith angle less than 70° are included as cloud shadowing at high view angles can decrease the OMI-derived LER.

methods introduced in Sect. 2.6. We note there is a spectral dependence in the difference between GLER and the OMI-derived LER. At 354 nm GLER is biased high compared to the OMI-derived LER, whereas no bias exists at 388 nm~~and at~~. For longer wavelengths of 440 nm and 446 nm, GLER are biased low compared to OMI-derived LER. As shown in Table 2, the GLER and the OMI-derived LER compare best in January at 388 nm where $R^2$ is ~~0.74~~ 0.76 and the bias is 0.002 ~~. For Vis wavelengths, there appears to be two distributions of data in the scatterplot, which could~~

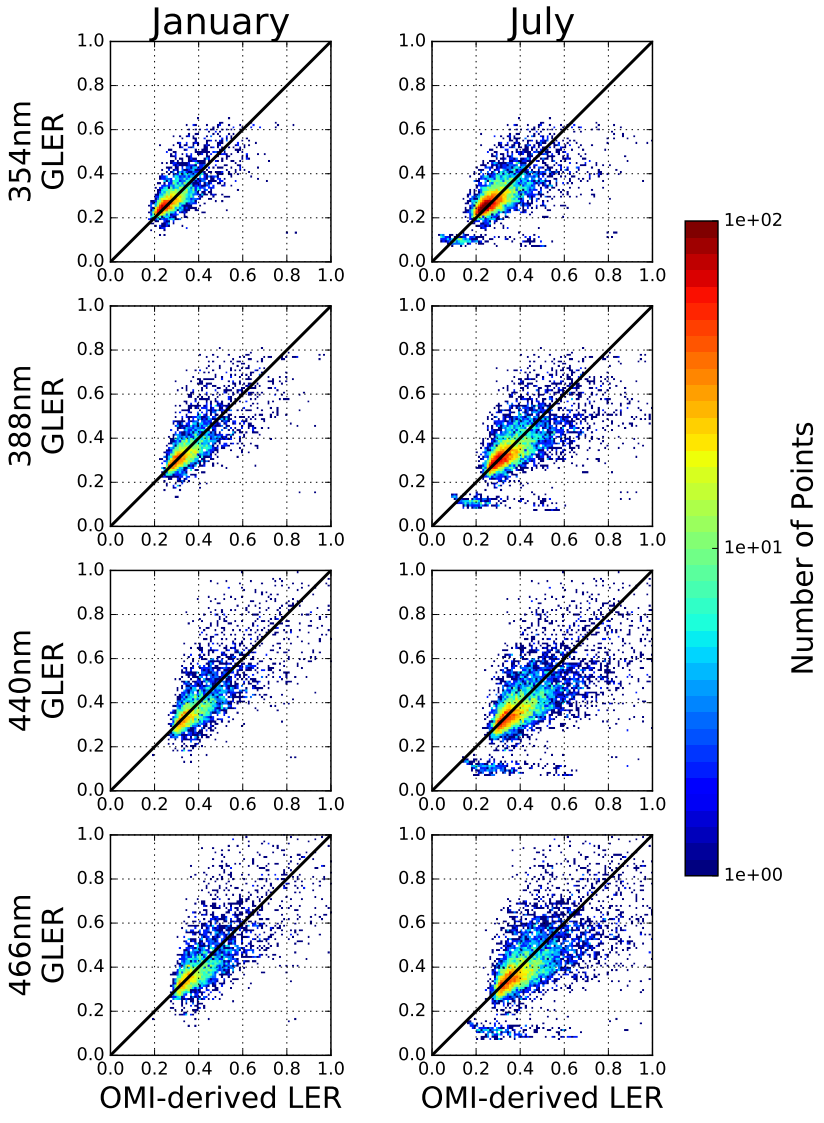


Fig. 2: Scatterplots of OMI-derived LER vs GLER for ~~January~~ two months in 2006 (January on left and July on right) for pixels with sun glint at 4 wavelengths (354 nm, 388 nm, 440 nm, and 466 nm). Data are for deep ocean with no screening for clouds or aerosols.

~~possibly be related to aerosols in the OMI measured data. These issues with aerosols will be further analyzed in Sect. 3.3.~~ with the raman based ECF (using the MODIS GCF $R^2$ is 0.60 and the bias is 0.007).

~~In general, the cloud screening methods produce similar results with only small differences that do not impact the overall evaluation. For the rest of the paper, the Raman ECF will be used for cloud screening as the Raman ECF shows better correlation than~~ Overall the comparison is better when using the raman based ECF cloud screen than when using the MODIS GCF~~which could simply be~~

Table 2: Statistical analysis of GLER vs OMI LER for non-sun glint scenes
January (July) 2006 deep ocean only with MODIS GCF = 0.0 (corresponds to 1st and 3rd columns of Fig. 1)

| Wavelength | Slope | $R^2$ | Mean Bias | RMSE | Npts |
|---|---|---|---|---|---|
| 354 nm | 0.52 (0.37) | 0.42 (0.28) | -0.005 (-0.008) | 0.014 (0.016) | 654,790 (549,152) |
| 388 nm | 0.69 (0.53) | 0.60 (0.46) | 0.007 (0.003) | 0.013 (0.012) | 654,790 (549,152) |
| 440 nm | 0.63 (0.43) | 0.56 (0.37) | 0.016 (0.013) | 0.019 (0.017) | 654,790 (549,152) |
| 466 nm | 0.64 (0.44) | 0.53 (0.36) | 0.016 (0.013) | 0.019 (0.017) | 654,790 (549,152) |

Table 3: Statistical analysis of GLER vs OMI LER for sun glint only scenes
January (July) 2006 deep ocean only~~(number of points = 4,344)~~

| Wavelength | Slope | $R^2$ | Mean Bias | RMSE | Npts |
|---|---|---|---|---|---|
| 354 nm | ~~0.70~~ 0.65 (0.51) | ~~0.55~~ 0.47 (0.41) | ~~-0.01~~ -0.004 (0.008) | ~~0.055~~0.065 (0.08) | 4,344 (8,326) |
| 388 nm | ~~0.74~~ 0.69 (0.52) | ~~0.56~~ 0.48 (0.41) | ~~-0.006~~ 0.006 (0.025) | ~~0.068~~ 0.081 (0.10) | 4,344 (8,326) |
| 440 nm | 0.75 (0.59) | 0.52 (0.43) | 0.013 (0.037) | 0.098 (0.12) | 4,344 (8,326) |
| 466 nm | 0.77 (0.62) | 0.53 (0.44) | 0.011 (0.036) | ~~0.010~~ 0.10 (0.13) | 4,344 (8,326) |

~~due to the fact that in 2006~~. This is expected given that there is a ~~15-minute overpass time difference between~~ 15 minute window between the Aqua and Aura overpass times in 2006 (becomes 7 minutes in 2009) leading to some change in cloud cover. It is also worth noting since OMI has a wider swath than MODIS, ~~MODIS~~ cloud retrievals are not available from MODIS for pixels on the edge of OMI swath (these pixels are not shown in Fig. 1). For these reasons the raman based ECF will be used for cloud screening in the rest of the paper.

In Fig. 2, the comparisons of GLER and OMI-derived LER are presented for data with sun glint. These data were not screened ~~for cloud or aerosols~~with cloud or aerosol retrievals, as strong glint can lead to artificial classification of aerosol or clouds in the retrieval algorithms. ~~It is evident that there are two main regions for the sun glint, a more general sun glint distribution with reflectivity between 0.2-0.4 and then a smaller distribution that exhibits extreme sun glint where LER reaches as high as 1.~~ As shown in Table 3, the bias between GLER and the OMI-derived LER is smaller for the data with sun glint than the sun glint-free data. For sun glint pixels, the bias is smaller at ~~longer~~ UV wavelengths where the water leaving radiance contributes the least. ~~Despite the smaller bias, $R^2$ is worse for the sun glint cases at around 0.55 due to the increased sensitivity of GLER to the wind speed for sun glint scenes.~~ For the brighter glint data, there is much more uncertainty and GLER is biased high compared with the OMI-derived LER. If the measured wind speed is too low, the model will overestimate the LER of the glint, whereas when the measured wind speed is too high, the model will underestimate the LER of glint. This sensitivity to the wind speed will be further

evaluated in Sect. 3.5. The small bias is possibly caused by aerosols which scatter or absorb the direct light causing a small dimming ~~affect~~ effect in the OMI glint data. This issue will be evaluated in Sect. 3.3.

### 3.2 Angular Behavior of GLER

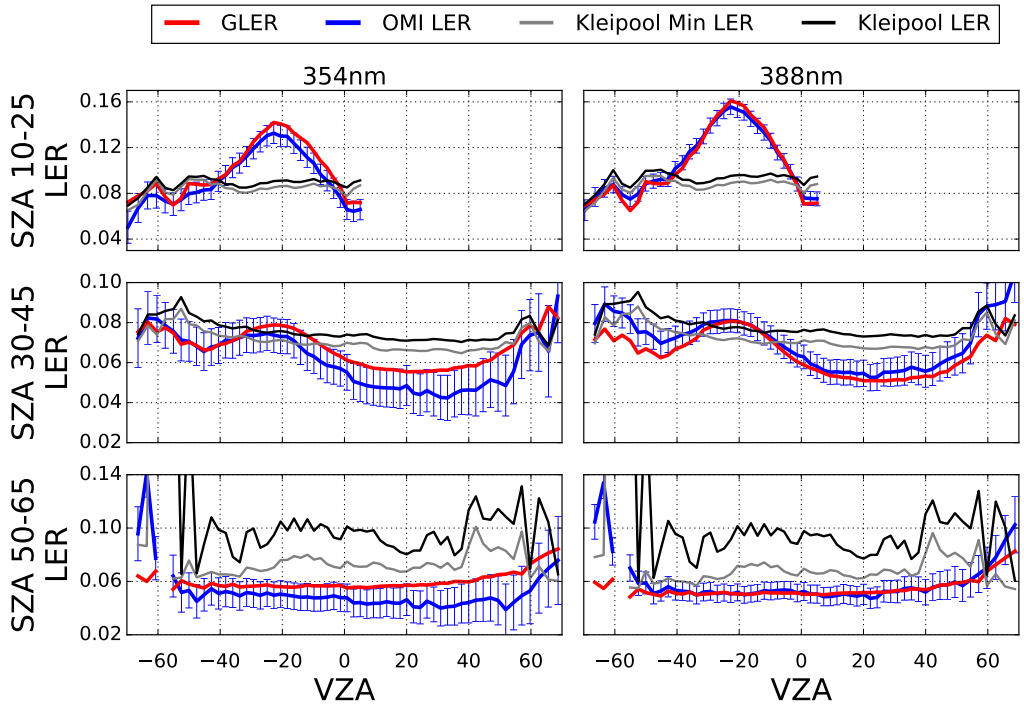


Fig. 3: January 2006 LER as a function of VZA for select SZA ranges at 354 nm and 388 nm over the Pacific Ocean (only deep ocean pixels considered). The blue error bars represent the 2% calibration uncertainty of OMI (Dobber et al., 2008). Negative VZAs represent the west side of the OMI swath (forward scattering), whereas positive VZAs represent the east side of the OMI swath (backward scattering). Data are screened for clouds with the ~~Raman~~ raman based ECF and aerosols are removed with the OMAERUV AI.

Figures 3 and 4 show a comparison of the cross-track dependence of GLER and OMI-derived LER along with the Kleipool LER climatology for a few solar zenith angle ranges screened for clouds using the ~~Raman~~ raman based ECF and screened for absorbing aerosols with the OMAERUV AI. GLER follows a similar cross-track pattern at various solar zenith angles as the OMI-derived LER that varies with wavelength. However, there is a bias between GLER and the OMI-derived LER which varies by wavelength. For Vis wavelengths, the OMI-derived LERs are biased hugh by as

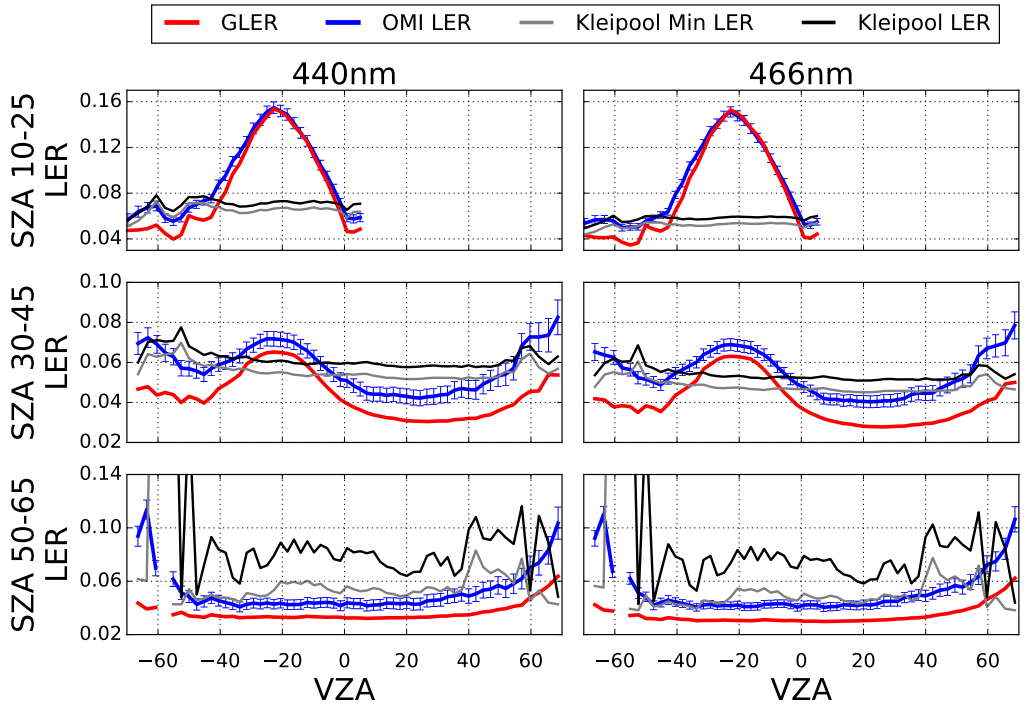


Fig. 4: Same as Fig. 3 but for 440 nm and 466 nm

much as 0.01-0.02 ~~high~~ compared to the GLER, whereas for UV wavelengths the bias is nearly zero at 388 nm and at 354 nm GLER is biased around 0.01 higher than the OMI measurements. In the UV channels, especially at 354 nm, the bias varies both with cross-track and solar zenith angle. ~~Outside of the sun glint, where water leaving radiance dominates the reflectance due to increased diffuse illumination, reflectivity decreases with increasing wavelength because pure water absorption increases with wavelength.~~

The Kleipool LER climatology compares well with the OMI-derived LER near nadir but does not capture any of the BRDF effects seen in both GLER and OMI-derived LER since it is a climatology that averages all viewing geometries. We note that there is a slight increase in Kleipool LER at higher view zenith angles, but this is simply due to the sampling used for this analysis. Compared to the OMI-derived LER, the Kleipool data have a cross-track-dependent difference of as much as 0.04 outside of the sun glint and 0.1 in the sun glint for UV wavelengths. The difference between Kleipool and the OMI-derived LER (0.01) is smaller for Vis wavelengths outside of the sun glint. At the higher solar zenith angles, the Kleipool monthly data appear to be adversely affected either by ice or residual cloud that was not fully removed from the Kleipool LER climatology. This is evident by the large bias compared with OMI-derived LER as well as the large variability coming

from spatial sampling.

### 3.3 Simulating GLER with Aerosols

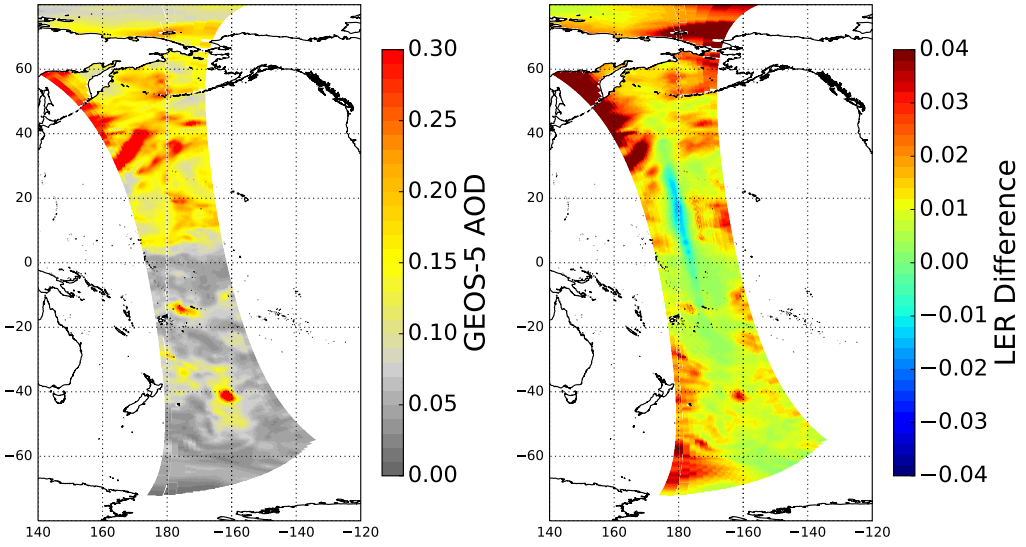


Fig. 5: Map showing the results from GLER aerosol simulation ~~for~~ on April 10, 2006 ~~Orbit 09229.~~ for orbit 9229. On the left is GEOS-5 470 nm AOD used in the simulation and on the right is change in GLER when the aerosol contribution is added to the simulations at 466 nm.

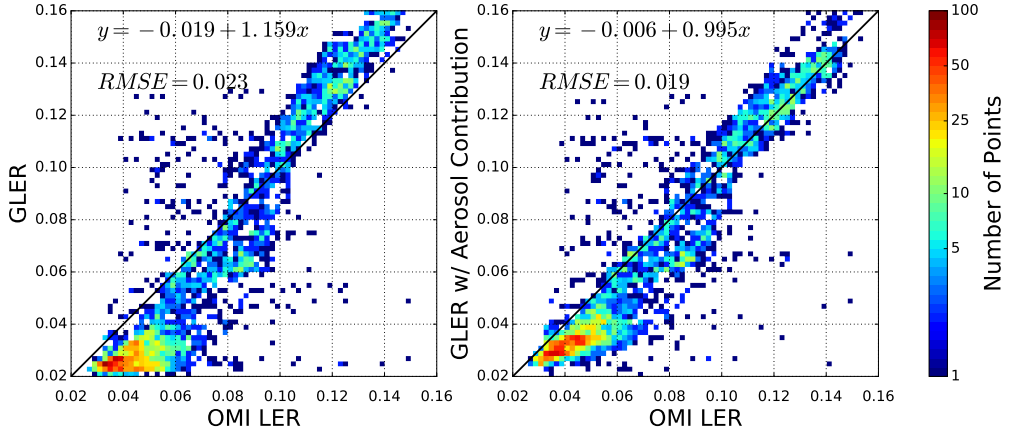


Fig. 6: Comparison of GLER versus OMI-derived LER for orbits on April 10, 2006 ~~Orbit 09229.~~ over the Pacific Ocean. On the left is GLER compared to OMI-derived LER at 466 nm, whereas on the right is GLER with contribution from aerosols vs OMI-derived LER for 466 nm. All data are filtered to remove clouds with the ~~Raman~~ raman based ECF

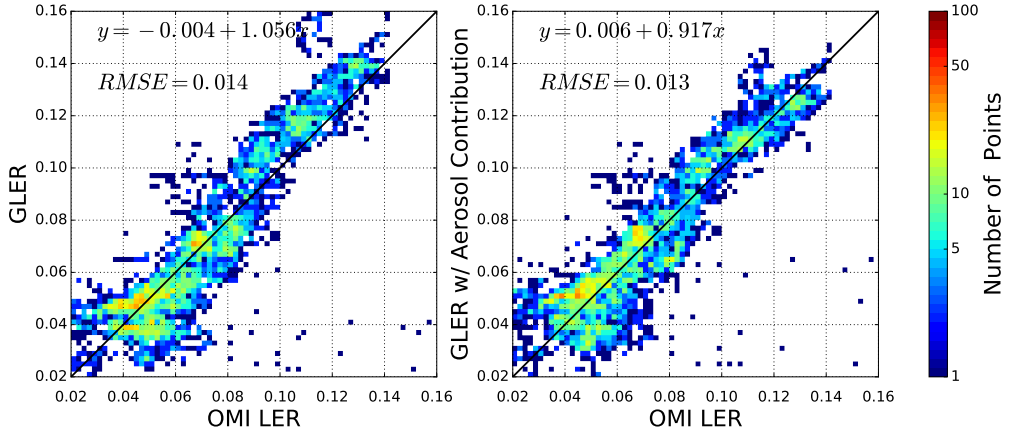


Fig. 7: Same as Fig. 6 but for 354 nm

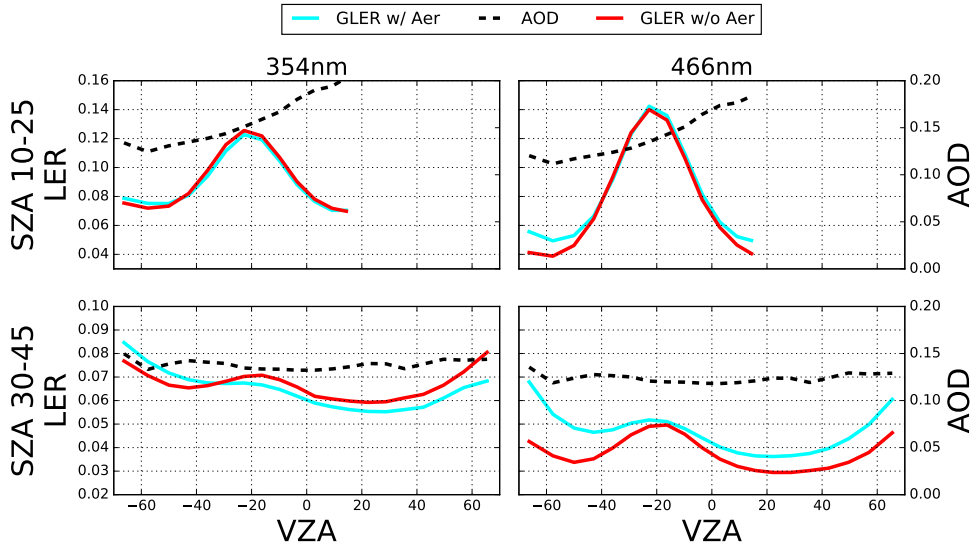


Fig. 8: LER as a function of VZA at 354 nm and 466 nm for orbits on April 10, 2006 ~~Orbit 09229. Data are cloud screened with~~ over the ~~Raman ECF, but have not been screened for aerosols~~Pacific Ocean. As in Fig. 3 negative VZAs represent the west side of the OMI swath whereas positive VZAs represent the east side of the OMI swath. Since only simulated data is shown, no cloud or aerosol screening is performed.

As noted in earlier sections, aerosols can have an impact on measured LER. For this reason, a simulation was performed to calculate GLER including the effect of aerosols. Aerosol-related input parameters to VLIDORT (layer AOD, single scattering albedo [SSA], and phase function) are from MERRA-2 aerosol reanalysis data which is produced using the GEOS-5 atmospheric model and

data assimilation system. MERRA-2 assimilates radiance data from a variety of satellite sensors which are then used to train a neural network to produce AOD which is calibrated to the Aerosol Robotic Network (AERONET) direct-Sun point measurements(Randles et al., 2017; Gelaro et al., 2017). The species-specific aerosol scattering ~~functions~~ matrices are characterized by six sets of generalized spherical function expansion coefficients generated from Mie theory.

The simulation was performed for ~~orbit 9229 on~~ April 10, 2006 over the central Pacific Ocean in order to determine the aerosol effect for a general background oceanic aerosol case. Figure 5 shows ~~that the AOD for this orbit ranged~~ the MERRA-2 AOD and the LER change due to added aerosols for orbit 9229 where AOD ranges from around 0.05 in the South Pacific gyre to larger than 0.4 in the northern Pacific. The impact of the aerosols on GLER ranges from a decrease in LER of 0.01 in sun glint to an increase in LER of greater than 0.04 outside of the glint, especially at higher viewing angles. Figures 6 and 7 show the comparison between GLER and the OMI-derived LER as well as a comparison between GLER with a contribution from aerosols and the OMI-derived LER.

In Fig. 6 the addition of aerosols at 466 nm increases the LER by about 0.01 over darker surfaces, whereas the brighter regions which have some sun glint contribution show a reduction in LER of around 0.01. The combination of these changes improves the ~~slope from 1.121~~ regression slope from 1.16 before considering aerosols ~~to 0.935~~ at 466 nm to 1.0 after aerosols are introduced. ~~There is also improvement of the root mean squared error (RMSE) which decreases from 0.026 to 0.02.~~ After accounting for aerosols, OMI-derived LER is still around 0.01 higher than GLER at 466 nm for darker surfaces. The brighter surfaces, however, which have some sun glint contribution, have little to no bias after accounting for aerosols. Figure 8 shows that aerosols increase GLER generally by 0.01-0.02, with the largest increase at large forward scattering viewing zenith angles.

At 354 nm the aerosol impact is not as significant as that seen for 466 nm with ~~on the whole~~ little to no change in the bias for darker surfaces and a reduction of around 0.01 for the brighter surfaces. In Fig. 8 there is a cross-track dependence in the aerosol contribution to GLER at 354 nm. For geometries with forward scattering (negative VZAs), the aerosol contribution can effectively increase the derived LER by 0.01 or more, whereas for backward scattering geometries (positive VZA) there is ~~little to no change~~a small decrease in LER. This view angle dependence of the aerosol impact would remove the ~~crosstrack dependent bias~~ view angle dependent bias between GLER and OMI-derived LER seen in Fig. 3~~resulting~~ . Therefore, applying the aerosol impact to Fig. 3 would result in GLER being approximately 0.01 higher than the OMI-derived LER at 354 nm for all view angles.

~~Overall~~ In this case study, we note that ~~at 466~~ an AOD of 0.1-0.15 ~~can increase LER by around 0.01 in the backscattering direction, while increasing~~ increased the LER by as much as ~~0.02~~ 0.01-0.02 at 466 nm, with the largest increase being in the forward scattering direction. At 354 nm, however, similar AOD values ~~have little impact in the back scattering~~ slightly decrease LER in the backward

scatter direction, but can increase LER by as much as 0.01 in the forward scattering direction. While this analysis was for only a specific case study, we note that the aerosol contribution likely accounts for some of the difference between GLER and the OMI-derived LER.

### 3.4 Inter-annual Variability of LER

Surface LER over the ocean can change day to day ~~depending on~~ with the chlorophyll concentration ~~which affects~~ affecting the water leaving radiance contribution ~~as well as due to~~ and changes in the wind speed ~~which can alter~~ altering the roughness of the water surface. There is also a seasonal variation in LER due to the changing viewing geometry of satellite measurements as the SZA changes through the year. In Figs. 9 and 10, GLER and OMI-derived LER are shown for the duration of the OMI mission to evaluate the ability of GLER to capture these variations. In this figure, data were selected for a region in the south Pacific gyre (180W-120W, 30S-Equator) as this region is generally free of strong aerosols and has relatively low cloud fractions. OMI row 10 is evaluated to avoid sun glint as well as to avoid the OMI row anomaly which impacts many of the OMI rows starting around ~~2009 (Levelt et al., 2018)~~2007 (Levelt et al., 2018; Schenkeveld et al., 2017). While this relatively small bias between GLER and the OMI-derived LER is evident, GLER does follow the same general trend as the OMI measured data.

Figure 10 shows there is about a 0.01 seasonal variation in the GLER and OMI-derived LER difference for all wavelengths which could possibly be due to seasonal changes in aerosols or seasonality in cirrus clouds that are too thin to be retrieved by the ~~Raman~~ raman based ECF. We note that in Fig. 10 there is a small downward trend in the difference between GLER and OMI-derived LER of at most 0.005 ~~LER~~in LER. At 354 nm a change of 0.005 LER corresponds to approximately 1% TOA radiance which is close to the 1-1.5% TOA radiance degradation noted by Schenkeveld et al. (2017). ~~This may be related to the downward drift in the OMI measurements which is known to be about 2% in TOA radiance over the duration of the mission.~~

### 3.5 Sensitivity to Chlorophyll and Wind Speed

Table 4: Sensitivity to wind speed

| Wavelength | Mean Abs Diff | Max Abs Diff |
|---|---|---|
| 354 nm | 0.0010 | 0.16 |
| 388 nm | 0.0013 | 0.21 |
| 440 nm | 0.0015 | 0.27 |
| 466 nm | 0.0016 | 0.30 |

In order to determine the uncertainty in GLER calculations, a sensitivity test was performed based

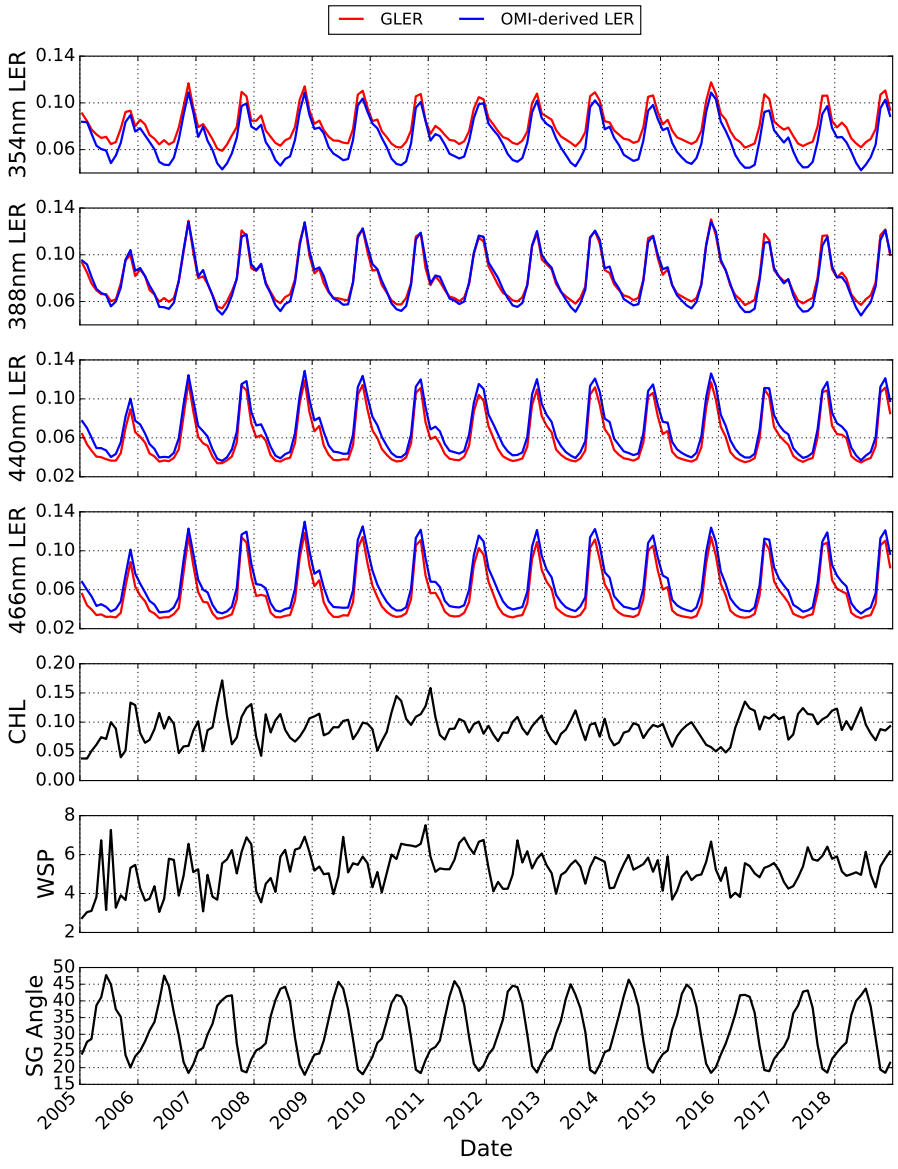


Fig. 9: Monthly mean of GLER and OMI-derived LER in equatorial Pacific ocean (180W-120W, 30S-0) for 4 wavelengths (354, 388, 440, and 466 nm) as a function of time for the OMI mission from row 10. Corresponding chlorophyll and wind speed measurements along with sun-glint angle used for GLER are shown in bottom three panels. Data are filtered to remove clouds with the ~~Raman~~ raman based ECF.

on the inputs of chlorophyll and wind speed. The wind speed measurements were perturbed +/- 1 m $s^{-1}$ as Wentz and Meissner (2000) note that is the uncertainty in their wind speed algorithm. The MODIS Ocean Color Team notes that the chlorophyll uncertainty varies regionally but can possibly be as high as 35% (Moore et al., 2009). We perturb chlorophyll by this 35% in order to gather an

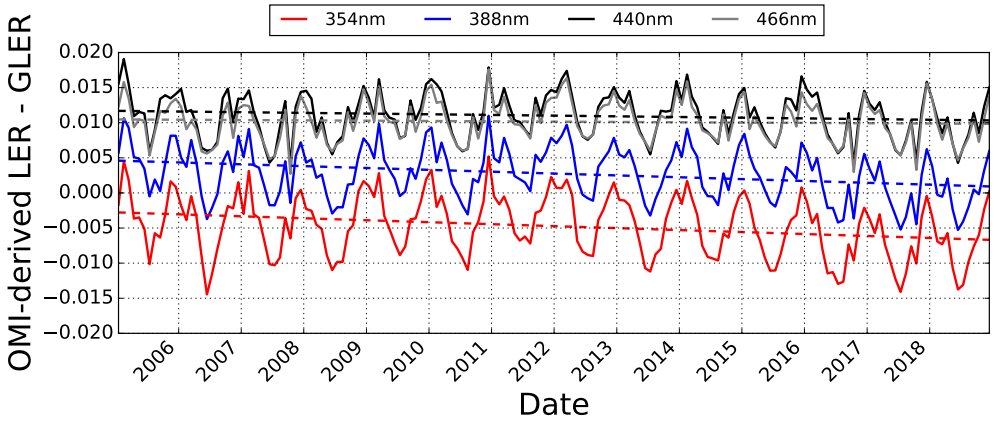


Fig. 10: Trend in the difference between the monthly mean GLER and the OMI-derived LER for the same location as in Fig. 9 at UV and Vis wavelengths for row 10. Data are filtered to remove clouds with the ~~Raman~~ raman based ECF.

Table 5: Sensitivity to chlorophyll

| Wavelength | Mean Abs Diff | Max Abs Diff |
|---|---|---|
| 354 nm | 0.0043 | 0.0067 |
| 388 nm | 0.0047 | 0.0087 |
| 440 nm | 0.0022 | 0.0047 |
| 466 nm | 0.0012 | 0.0019 |

Table 6: Sensitivity to wind speed and chlorophyll

| Wavelength | Mean Abs Diff | Max Abs Diff |
|---|---|---|
| 354 nm | 0.0044 | 0.17 |
| 388 nm | 0.0049 | 0.21 |
| 440 nm | 0.0028 | 0.27 |
| 466 nm | 0.0021 | 0.30 |

absolute bound of GLER to the chlorophyll input. We place an absolute lower bound on the wind speed in our calculations of 0.4 $\mathrm{m\,s^{-1}}$ and a lower bound of 0.01 of $\mathrm{mg\,m^{-3}}$ on the chlorophyll ~~data sets~~ datasets as measurements of these input below these lower bounds are unrealistic and could lead to large errors in calculation of GLER. In Tables 4, 5, and 6 the magnitude of the mean and max differences are reported in units of LER.

As seen in Table 4 the average wind speed sensitivity is quite small at around 0.0015, but the maximum sensitivity can become as high as 0.3 due to the high sensitivity of sun glint to wind speed. This is because for extreme sun glint cases a small roughness in the ocean surface will lead

to increased scattering of light which will significantly diminish the strength of the glint. It is worth noting that while such roughness decreases the strength of the glint, it will increase the overall size of the region affected by sun glint due to the scattering of light at the ocean surface. The wind speed sensitivity decreases with decreasing wavelength because the fraction of the direct solar light which is responsible for sun glint decreases for shorter wavelengths where the contribution of the diffuse light increases due to Rayleigh scattering.

In Table 5 the chlorophyll sensitivity is shown to be much smaller than the wind speed sensitivity. In contrast with the wind speed sensitivity, the chlorophyll sensitivity is largest at UV wavelengths because the CDOM absorption, which rises with increasing chlorophyll according to the Case 1 water model, exponentially increases for shorter wavelengths.

~~When both~~ To determine the combined effect, we additionally calculated GLER perturbing both the wind speed and chlorophyll ~~sensitivity are combined,~~ for the four possible combinations. Table 6 shows the mean difference from the combined sensitivity analysis in GLER is similar to that obtained ~~with just the chlorophyllsensitivity~~by only perturbing the chlorophyll. The maximum difference from the combined sensitivity test, however, is similar to that of the wind speed perturbation. This is ~~likely~~ because while the wind speed has a significant impact on sun glint, only a small fraction of OMI pixels are impacted by glint.

### 3.6 Additional Sources of Uncertainty

We note that in addition to the sensitivities from the input data, uncertainties also result from the modeling of the GLER as well as the OMI data used for the evaluation. One possible source of uncertainty is the water leaving radiance model being used in the calculations. Here we implement a Case 1 water model that is assumed to be representative of the global oceans with dependence only on chlorophyll. Szeto et al. (2011), however, showed that the world's oceans are optically variable and that optical parameters such as chlorophyll absorption vary even for Case 1 open ocean. Work by Lee et al. (2006) similarly showed that large deviations exist from the presumed Case 1 water model due to uncertainty in the optical properties used to parameterize the models. They determined that the SeaWiFS remote sensing reflectance retrievals at 555 nm for Case 1 water have a deviation of +/- 50% from that of a Case 1 bio-optical property model.

Our simulations do not include any vibrational-Raman scattering effects which can increase the water leaving radiance. Westberry et al. (2013) show that Raman scattering can impact the water leaving radiance in Vis wavelengths as much as 4-7% for low chlorophyll concentrations.

In Sect. 3.3 is it shown that aerosols can increase the LER derived from OMI. Uncertainty in AOD used for this analysis could have an appreciable impact on the evaluation results. Randles et al. (2017) compare the MERRA-2 550 nm AOD with the Maritime Aerosol Network (MAN) and

find the MERRA-2 AOD to be biased low by 0.009 with large spread in the comparison which they note could be due to the uncertainty of the MAN AOD of +/- 0.02. Even though the AOD uncertainties are small, we have shown that even a 0.05-0.1 AOD increase can increase 466 nm LER by 0.005-0.01.

With regard to the OMI measurements, uncertainty could arise from the cloud screening of the OMI measurements as retrieval of cloud properties can become difficult for thin cirrus clouds, which are especially prevalent over the western Pacific (Nazaryan et al., 2008). It has been shown that such contamination can actually increase MODIS AOD retrievals by 0.015-0.025 (Kaufman et al., 2005). As previously mentioned, there is also up to a 2% TOA radiance absolute calibration uncertainty with the OMI measurements (Dobber et al., 2008) which can lead to an uncertainty of around 0.01-0.02 in LER in the UV and up to 0.005 LER in the Vis. Several OMI algorithm teams apply adjustments to remove residual error in viewing angle dependence in the OMI measurements by looking at Earth radiances over land. When these corrections were applied in our evaluation of GLER, we found the difference between GLER and the OMI measurements in the UV and Vis was reduced.

Given the uncertainties listed above, we believe differences between GLER and OMI measurements are likely caused by some combination of these factors. It is possible that these factors vary with wavelength. For example, we have shown that aerosols have a greater impact at 440 nm and 466 nm, whereas other factors such as chlorophyll uncertainty are more important at 354 nm and 388 nm where the water leaving radiance contributes more than the direct reflectance.

## 4 Conclusion

Previous work Qin et al. (2019) introduced the GLER product for land surfaces based on BRDF input from MODIS. In this paper we evaluate a surface LER product called GLER which accounts for the ocean surface BRDF effects at UV and Vis wavelengths. Surface roughness is modeled using the Cox-Munk slope that depends on wind speed measurements from the AMSR-E and SSMIS instruments. A contribution of water leaving radiance is also included which is based on chlorophyll input from MODIS.

We evaluated the GLER product over water by comparing with OMI-derived LER at UV and Vis wavelengths. The BRDF effect in the OMI-derived LER is captured well with the GLER data at Vis wavelengths~~and small view angle dependence in the difference for UV wavelengths which~~. At UV wavelengths, however, the difference between OMI-derived LER and GLER varies some with viewing angle. This UV effect could possibly be explained by the ~~anisotropic scatter~~ scattering of aerosols. There is, however, a bias between GLER and the OMI-derived LER which is ~~less~~ no more than 0.01 ~~LER~~ after accounting for the effect of aerosols.

We note the GLER data capture the seasonality and inter-annual variability seen in the OMI

measurements that may be caused by variations in the viewing angles as well as changes in the chlorophyll and wind speed data due to meteorological phenomena. The bias between GLER and OMI-derived LER could be caused by a combination of ~~things~~ factors including small calibration errors in the OMI-derived LER, deviations in the OMI measurements from the Case 1 water model, and residual thin ~~cloud~~ clouds that are difficult to screen.

There are several possible applications for the GLER product. It can be used to replace climatological LER's currently used by many cloud, trace gas, and aerosol algorithms. Additionally, GLER can be used as a tool to evaluate satellite calibration to detect possible drift or striping in instrument retrievals. In future missions such as PACE, GLER can be adapted to perform retrievals of water leaving radiance at UV and Vis wavelengths.

In future work we plan to implement a Case 2 water model for turbid and coastal waters as well as replace our LUT approach with a neural network approach to reduce the computational time to produce the GLER product.

## Appendix A Description of the VSLEAVE Water-Leaving Radiance Model

In this Appendix, we give details of the water-leaving radiance scheme included in the VSLEAVE supplement to VLIDORT Version 2.8. Section A1 of this appendix deals with the basic water leaving formulation, while Sect. A2 deals with the ocean optics model. In particular, the material in Sect. A2 is based on the work of Sayer et al. (2010), which has a comprehensive review of semi-empirical marine optics formula, and a companion paper Sayer et al. (2017), the latter containing important updates to the optics model. The treatment is for Case 1 waters.

### A1 Water-Leaving Radiance Model

Here we summarize the computation of water-leaving radiances using the VSLEAVE supplement to VLIDORT. A full description of the VLIDORT VSLEAVE supplement used here may be found in Spurr et al. (2019). Water-leaving output from VSLEAVE consists of three terms which are sun-normalized radiances. The first is a direct term $L_{w,direct}(\mu, \mu_o, \phi)$ which is the water leaving radiance for solar illumination angle $\theta_0$ and cosine $\mu_0 = \cos(\theta_o)$ going into the viewing direction with zenith angle $\theta$ and $\mu = \cos\theta$ and the relative azimuth angle $\phi$ between the solar and viewing directions.

The other two water-leaving radiance outputs may be written $L_{w,m}(\mu, \mu_0)$ and $L_{w,m}(\mu_i, \mu_0)$, where $\mu_i (i = 1, \ldots N_d)$ are the discrete-ordinate polar cosines, and $m$ is the Fourier component index, $m = 0, 1, \ldots 2N_d - 1$. These are diffuse-term contributions: $L_{w,m}(\mu_i, \mu_0)$ is required for the inclusion of surface leaving in the diffuse-scattering boundary condition at surface, while the

term $L_{w,m}(\mu,\mu_0)$ is required for post-processing of the discrete ordinate solution. Fourier terms arise from cosine-azimuth expansions of the full functions: $L_{w,direct}(\mu,\mu_0,\phi) = L_{w,0}(\mu,\mu_0) + 2\sum_{m=1}^{\infty} L_{w,m}(\mu,\mu_0)\cos(m(\phi))$. In the discrete-ordinate approximation with $N_d$ streams, we can only use $2N_d - 1$ components in this sum. In the post-processing, it is more accurate to use the complete term $L_{w,direct}(\mu,\mu_0,\phi)$ itself in place of the (less-accurate) Fourier-series truncation, and this "exact-term correction" is the default in VSLEAVE. In this case, Fourier terms $L_{w,m}(\mu,\mu_0)$ are not needed. Note that we will always need the Fourier components $L_{w,m}(\mu_i,\mu_0)$ for the diffuse-field calculation. However, when there is no azimuth dependence, only $L_{w,0}(\mu_i,\mu_0)$ for $m = 0$ survives. In this study we consider an anisotropic distribution of the water-leaving contribution, but the model can also generate it as an isotropic term $L_{w,iso}(\mu_0)$ which depends only on the incoming solar direction (no azimuth dependence, all outgoing directions equal), in which case $L_{w,m}(\mu,\mu_0) = 0(m \geq 1)$ and $L_{w,0}(\mu,\mu_0) = L_{w,iso}(\mu_0)$ for all outgoing polar directions $\mu$ , and also $L_{w,direct}(\mu,\mu_0,\phi) = L_{w,iso}(\mu_0)$. The current default for VSLEAVE is for an unpolarized azimuth-independent formalism. Thus only the intensity component of the water-leaving Stokes vector is non-zero, and there is no azimuthal dependence.

Water-leaving radiance may be written as

$$L_w(\mu,\mu_0,\phi) = L_w^*(\mu,\mu_0,\phi;\mathrm{Chl},\mathrm{V})\,T_{atm}(\mu_0)\,, \tag{A1}$$

for any given combination of angles, where the transmittance $T_{atm}(\mu_0)$ depends only on the solar angle, and $L_w^*(\mu,\mu_0,\phi,\mathrm{Chl},\mathrm{V})$ is computed from the marine optical properties using a semi-empirical model which depends explicitly on the chlorophyll concentration and wind speed $V$. The ocean-optics model for the determination of $L_w^*$ is described below.

### A2 Ocean-Optics Model

Though the longest wavelength in the GLER product is presently 466 $\mathrm{nm}$, we describe our model of ocean optics over a wider spectral range below as the model has applications in aerosol and ocean color studies where the longer visible and near-infrared wavelengths are typically used. The water absorption $\alpha_W(\lambda)$ coefficients have been linearly interpolated from a table of values at every 5 $\mathrm{nm}$ from 200-900 $\mathrm{nm}$ constructed from a number of literature sources. These are Quickenden and Irvin (1980), interpolated with Lee et al. (2015) between 325 and 345 $\mathrm{nm}$; (2) 350-550 $\mathrm{nm}$ from Lee et al. (2015); Pope and Fry (1997) for 555-725 $\mathrm{nm}$; Hale and Querry (1973), table 1, for 725-900 $\mathrm{nm}$ (the latter with 25 $\mathrm{nm}$ increments linearly interpolated to 5 $\mathrm{nm}$ values]. Table entries provided as extinction coefficients $k_W$ are converted using $\alpha_W(\lambda) = \frac{4\pi k_W}{\lambda}$, where wavelengths are in $\mathrm{m}$ and extinctions in $\mathrm{m}^{-1}$.

The chlorophyll absorption $\alpha_{ph}(\lambda)$ comes from two sources. The first source (in the range 300-400 $\mathrm{nm}$) relies on linear interpolation of two sets of coefficients $\{a_1(\lambda), b_1(\lambda)\}$ given at 10 $\mathrm{nm}$

intervals in this range (Vasilkov et al., 2005). The absorption is given by

$$\alpha_{Ph}\left(\lambda, \mathrm{Chl}\right) = \mathrm{Chl} \cdot \mathrm{a}_1\left(\lambda\right) \cdot \mathrm{Chl}^{-\mathrm{b}_1(\lambda)}, \tag{A2}$$

where Chl is the chlorophyll concentration and $\lambda$ is wavelength. The value at 300 nm is used for all $\lambda < 300$ nm. The second source (over the range 400-720 nm) is based on linear interpolation of two sets of coefficients $a_2(\lambda), b_2(\lambda)$ at 10 nm intervals (Lee et al., 2005). The absorption formula in this regime is given by

$$\alpha_{Ph}\left(\lambda, \mathrm{Chl}\right) = \left[a_2\left(\lambda\right) + b_2\left(\lambda\right) ln\left(a_{440}\right)\right] a_{440}, \tag{A3}$$

where $a_{440} = 0.06 \cdot \mathrm{Chl}^{0.65}$ (Morel and Maritorena, 2001). The value at 720 nm is used for all $\lambda > 720$ nm. The CDOM absorption is given by Morel and Maritorena (2001):

$$\alpha_{CDOM}\left(\lambda, \mathrm{Chl}\right) = 0.2 \cdot \left(\alpha_w(440\,\mathrm{nm}) + 0.06 \cdot \mathrm{Chl}^{0.65}\right) exp\left[-0.014\left(\lambda - 440\right)\right], \tag{A4}$$

where $\alpha_w(440\,\mathrm{nm}) = 0.00635$ and $\lambda$ is in nm. The complete absorption is then

$$\alpha_{TOT}\left(\lambda, \mathrm{Chl}\right) = \alpha_W\left(\lambda\right) + \alpha_{Ph}\left(\lambda, \mathrm{Chl}\right) + \alpha_{CDOM}\left(\lambda, \mathrm{Chl}\right). \tag{A5}$$

We use the following formula for the backscattering coefficient, assuming it is half of the scattering coefficient for pure water Rayleigh scattering, as described in Morel et al. (2007):

$$b_W\left(\lambda\right) = 0.0028\left(\frac{420}{\lambda}\right)^{4.3}, \tag{A6}$$

with $\lambda$ in nm. This For the particulate matter backscattering coefficient, we use the following from Morel and Maritorena (2001):

$$b_{Ph}\left(\lambda, \mathrm{Chl}\right) = b_{Pb}\left(\mathrm{Chl}\right) \beta_{bbp}\left(\mathrm{Chl}, \lambda\right) \tag{A7}$$

$$b_{Pb}\left(\mathrm{Chl}\right) = 0.416 C^{0.766};\ \beta_{bbp}\left(\mathrm{Chl}, \lambda\right) = 0.002 + 0.01\left[0.5 - 0.25 log_{10}\mathrm{Chl}\right]\left(\frac{\lambda}{550}\right)^{V}, \tag{A8}$$

where the exponent $V = 0$ for $\mathrm{Chl} > 2$ , and $V = 0.5\left[log_{10}\mathrm{Chl} - 0.3\right]$ for $\mathrm{Chl} \leq 2$. The complete backscattering is then

$$b_{TOT}\left(\lambda, \mathrm{Chl}\right) = b_W\left(\lambda\right) + b_{ph}\left(\lambda, \mathrm{Chl}\right). \tag{A9}$$

In the original formulation of water-leaving radiance in VLIDORT, the following formula was used to obtain the basic ocean-surface reflectance (Morel and Gentili, 1992):

$$R\left(\mathrm{Chl}, \lambda, \mu_0\right) = f\left(\mu_0\right) R_{TOT}\left(\lambda, \mathrm{Chl}\right) \equiv f\left(\mu_0\right) \frac{b_{TOT}\left(\lambda, \mathrm{Chl}\right)}{a_{TOT}\left(\lambda, \mathrm{Chl}\right)} \tag{A10}$$

$$f(\lambda, \mathrm{Chl}, \theta_0) = d_0 - d_1\eta - d_2\eta^2 + (d_3\eta - d_4)\,\mu_0; \qquad \eta = \frac{b_W(\lambda)}{b_{TOT}(\lambda, \mathrm{Chl})}. \tag{A11}$$

Here, $f(\lambda, \mathrm{Chl}, \theta_0)$ is given with 5 constants $\{ d_0, d_1, d_2, d_3, d_4 \} = \{$ 0.6279, 0.0227, 0.0513, 0.2465, 0.3119 $\}$ , and $\mu_0 = \cos(\theta_0)$ is the cosine of the solar zenith angle. In order to assign the water-leaving radiance, the complete reflectance term is given by

$$R'(\mathrm{Chl}, \lambda, \mu_0) = \frac{R(\mathrm{Chl}, \lambda, \mu_0)}{1 - \omega R(\mathrm{Chl}, \lambda, \mu_0)}. \tag{A12}$$

Here, albedo $\omega = 0.485$, using the value in Austin (1974). The isotropic water-leaving radiance is then obtained after passage through the air-ocean interface:

$$S_{iso}(\mathrm{Chl}, \lambda, \mu_0) \approx \frac{\mu_0}{\pi} T_{Surf}(\theta_0) \frac{R'(\mathrm{Chl}, \lambda, \mu_0)}{|n_w|^2}. \tag{A13}$$

Here, $n_w$ is the relative refractive index of water to air. For the flat surface case, the air-water boundary transmittance $T_{Surf}(\theta_0)$ is often set to 1.0. In practice we use Fresnel optics to compute this quantity; values are typically 0.96 or more, depending on the value of $\theta_0$. In the rough surface case, $T_{Surf}(\theta_0)$ may be computed using glitter calculations based on Gaussian probability wave-facet distributions characterized by wind-speed and direction.

The above formulation does not account for the atmospheric transmitted flux $T_{atm}(\theta_0)$ at the ocean surface, a quantity which is propagated through the interface. In the previous formulation, the ratio $\frac{T_{atm}(\theta_0)}{Q}$ was made implicit in the factor $\frac{\mu_0}{\pi}$ appearing in ~~Eqn. A13~~Eq. ( A13). Also, we replace the $f(\lambda, \mathrm{Chl}, \theta_0)$ calculation with the direction-dependent ratio $\rho \equiv f/Q$ from Morel and Gentili (1996); Morel et al. (2002). The water-leaving radiance is then:

$$S(\mathrm{Chl}, \lambda, \theta_0, \mu, \varphi) = \mu_0 T_{atm}(\theta_0) T_{Surf}(\theta_0) \frac{R^*(\mathrm{Chl}, \lambda, \theta_0, \mu, \varphi)}{|n_w|^2} \tag{A14}$$

$$R^*(\mathrm{Chl}, \lambda, \theta_0, \mu, \varphi) = \frac{\rho(\mathrm{Chl}, \lambda, \theta_0, \mu, \varphi) R_{TOT}(\lambda, \mathrm{Chl})}{1 - \omega f(\mathrm{Chl}, \lambda, \theta_0) R_{TOT}(\lambda, \mathrm{Chl})}, \tag{A15}$$

where $R_{TOT}(\lambda, \mathrm{Chl})$ is as defined in ~~Eqn. A10~~Eq. ( A10), and $\rho$ is the ratio $f/Q$. We use a tabulated form of the ratio $f/Q$ in our calculations.

In order to obtain an isotropic surface leaving radiance, we derive a quantity $\bar{\rho}(\mathrm{Chl}, \lambda, \theta_0)$ from the $f/Q$ tables by averaging over all outgoing zenith and relative azimuth angles, $\theta$ and $\phi$ , then interpolating linearly with wavelength $\lambda$ , followed by cubic spline interpolation and linear interpolation with the solar angle cosine $\mu_0$ and with the logarithm of the chlorophyll concentration. Spline interpolation is necessary because we want smooth and continuous derivatives with respect to Chl when considering linearization, as discussed below. The quantity $\bar{\rho}(\mathrm{Chl}, \lambda, \theta_0)$ then defines the isotropic water-leaving contribution through:

$$S_{iso}(\mathrm{Chl}, \lambda, \theta_0) = \mu_0 T_{atm}(\theta_0) T_{Surf}(\theta_0) \frac{\bar{R}^*(\mathrm{Chl}, \lambda, \theta_0)}{|n_w|^2} \tag{A16}$$

$$\bar{R}^{*}\left(\mathrm{Chl},\lambda,\theta_0\right)=\frac{\bar{\rho}\left(\mathrm{Chl},\lambda,\theta_0\right)R_{TOT}\left(\lambda,\mathrm{Chl}\right)}{1-\omega f\left(\mathrm{Chl},\lambda,\theta_0\right)R_{TOT}\left(\lambda,\mathrm{Chl}\right)}. \tag{A17}$$

The azimuth dependence is very weak in the $f/Q$ tables, and we have omitted this dependence in the surface leaving formulation. However, we can derive non-isotropic surface-leaving $f/Q$ values by interpolating table entries with the cosine of the outgoing angle $\mu$. The resulting table extractions are then $\tilde{\rho_v}\left(\mathrm{Chl},\lambda,\theta_0,\mu_\mathrm{v}\right)$ and $\tilde{\rho_d}\left(\mathrm{Chl},\lambda,\theta_0,\mu_\mathrm{d}\right)$ for each viewing angle $\mu_v$ and discrete ordinate stream $\mu_d$; these quantities are azimuth-averaged. We then have

$$S_v\left(\mathrm{Chl},\lambda,\theta_0,\mu_\mathrm{v}\right)=\mu_0 T_{atm}\left(\theta_0\right)T_{Surf}\left(\theta_0\right)\frac{R_v^{*}\left(\mathrm{Chl},\lambda,\theta_0,\mu_\mathrm{v}\right)}{|n_w|^2} \tag{A18}$$

$$R_v^{*}\left(\mathrm{Chl},\lambda,\theta_0,\mu_\mathrm{v}\right)=\frac{\tilde{\rho_v}\left(\mathrm{Chl},\lambda,\theta_0,\mu_\mathrm{v}\right)R_{TOT}\left(\lambda,\mathrm{Chl}\right)}{1-\omega f\left(\mathrm{Chl},\lambda,\theta_0\right)R_{TOT}\left(\lambda,\mathrm{Chl}\right)}, \tag{A19}$$

and similarly for the discrete ordinate directions.

In the rough-surface case, the above analysis for the ocean reflectance still holds, but now we need to generate glitter-dependent transmission terms through the water-air interface, both for the incoming solar directions $\overrightarrow{T}_{aw}(\theta_0)$, and for outgoing line-of-sight $\overleftarrow{T}_{wa}(\theta_0,\mu_v)$ and discrete-ordinate $\overleftarrow{T}_{wa}\left(\theta_0,\mu_d\right)$ directions respectively. Thus for instance, the rough surface water-leaving term for a viewing angle $\mu_v$ is

$$S_{v,RS}\left(\mathrm{Chl},\lambda,\theta_0,\mu_\mathrm{v}\right)=\mu_0 T_{atm}\left(\theta_0\right)\overrightarrow{T}_{aw}\left(\theta_0\right)\frac{R_v^{*}\left(\mathrm{Chl},\lambda,\theta_0,\mu_\mathrm{v}\right)}{|n_w|^2}\overleftarrow{T}_{wa}\left(\theta_0,\mu_v\right), \tag{A20}$$

by analogy with ~~Eqn. A18 and using Eqn. A19~~Eq. ( A18) and using Eq. ( A19).

## Appendix B Coupling of VLIDORT and VSLEAVE

The simplest approximation to $T_{atm}\left(\mu_0\right)$ is the *decoupled* scenario where the transmittance has no dependence on ocean properties. In this case, we drop the $T_{atm}\left(\mu_0\right)$ term from the main VSLEAVE result in ~~Eqn. A1~~ Eq. ( A1) above, and then re-introduce $T_{atm}\left(\mu_0\right)$ from an internal computation in the main VLIDORT model. The direct transmittance $T_{direct}(\mu_0)=\exp[-\tau_{atm}/\mu_0]$ where $\tau_{atm}$ is the total atmospheric vertical optical depth; a closer value which includes a diffuse transmittance component is

$$T_{atm}\left(\mu_0\right)=exp\left[-\frac{1}{2}\frac{\tau_{atm}}{\mu_0}\right]. \tag{B1}$$

This equation was adapted from a similar formula in Gordon and Wang (1994). Equation B1 is easy to implement in VLIDORT. A more accurate expression may be obtained in certain cases by using a pre-calculated look-up table of $T_{atm}(\mu_0)$ values, computed offline with VLIDORT in a Rayleigh

atmosphere over a 270-900 nm wavelength range, and for a number of $\theta_0$. However, $T_{atm}(\mu_0)$ is still decoupled from the VSLEAVE water-leaving radiance output.

The coupling scheme works as follows. From ~~Eqn. A1~~Eq. ( A1), we write

$$L_w(\mu,\mu_0) = L_w^*(\mu,\mu_0)\,T^{\downarrow}(\mu_0)\,, \tag{B2}$$

where $T^{\downarrow}(\mu_0)$ is the total (direct and diffuse) downwelling atmospheric transmittance at the ocean surface, and $L_w^*(\mu,\mu_0)$ is the water-leaving radiance from VSLEAVE computed with unit transmittance. Here, $\mu_0$ is the solar zenith cosine, and $\mu$ any outgoing stream direction; we assume azimuth-independence.

To find the coupling adjustment for $T^{\downarrow}(\mu_0)$ , we an initial estimate $T_0^{\downarrow}(\mu_0)$ which could be the quantity in ~~Eqn. B1~~ Eq. ( B1) above; another value which we have tried is $T_0^{\downarrow}(\mu_0) = \frac{3}{2}T_{Direct}(\mu_0)$. With this starting value, we then have an adjusted water-leaving radiance $L_0(\mu,\mu_0) = L_w^*(\mu,\mu_0)\,T_0^{\downarrow}(\mu_0)$ which is then input to a Fourier-zero (azimuth independent) VLIDORT radiative transfer (RT) computation. From this RT computation we then derive an updated total downwelling transmittance $T_1^{\downarrow}(\mu_0)$, which in turn provides an updated water-leaving input $L_1(\mu,\mu_0) = L_w^*(\mu,\mu_0)\,T_1^{\downarrow}(\mu_0)$. We repeat the Fourier-zero VLIDORT radiative transfer calculation with this new input, yielding a new result $T_2^{\downarrow}(\mu_0)$ for the transmittance, and a new water-leaving value $L_{w,2}(\mu,\mu_0)$. This iteration is stopped when the relative difference in the value of $T^{\downarrow}(\mu_0)$ between two iterations is less than some small convergence criterion. We have found that convergence is rapid: typically only 3 iterations are needed for convergence at the level of $10^{-6}$.

It is not necessary to carry out a full Fourier calculation for every step. The discrete-ordinate homogeneous solutions and particular integrals do not depend on the surface-leaving radiance, and they need to be established just once from the initial Fourier-zero computation. Also, the complete discrete-ordinate solution is determined through the linear-algebra boundary value problem (BVP) $\mathbf{Ax} = \mathbf{B}$, where matrix $\mathbf{A}$ is constructed entirely from the homogeneous solutions to the radiative transfer equation (RTE), $\mathbf{x}$ is the vector of unknown homogeneous-solution integration constants, and vector $\mathbf{B}$ is constructed from the layer particular integrals and also contains the surface boundary condition appropriate for water-leaving. Once the matrix inverse $\mathbf{A}^{-1}$ is found, the BVP solution is obtained through straightforward back-substitution: $\mathbf{x} = \mathbf{A}^{-1}\mathbf{B}$. Thus, the first guess for water leaving input $L_0(\mu,\mu_0)$ will give rise to column vector $\mathbf{B}_0$ , with corresponding solution $\mathbf{x}_0 = \mathbf{A}^{-1}\mathbf{B}_0$. From the discrete-ordinate solution based on $\mathbf{x}_0$ , we then derive the next transmittance estimate $T_1^{\downarrow}(\mu_0)$ , then form the next-guess water-leaving input $L_{w,1}(\mu,\mu_0)$ and associated column vector $\mathbf{B}_1$ , from which we get the next solution $\mathbf{x}_1 = \mathbf{A}^{-1}\mathbf{B}_1$ , and so on. All column vectors $\mathbf{B}_p$ are similar only the surface-leaving entries are different. Thus the coupling adjustment is tantamount to a series of back substitutions, and this represents very little extra computation load compared with the main radiative transfer equation, finding the inverse $\mathbf{A}^{-1}$. A three-iteration calculation is

approximately 2% slower than a standard one.

Computation of the diffuse downwelling transmittance comes through the discrete-ordinate result:

$$T^{\downarrow}(\mu_0) = T^{\downarrow}_{diffuse}(\mu_0) + T^{\downarrow}_{direct}(\mu_0); \quad T^{\downarrow}_{diffuse} = \frac{2\pi}{\mu_0}\sum_{\alpha=1}^{n_d} I^{\downarrow}_{\alpha}\mu_\alpha c_\alpha \tag{B3}$$

$$I^{\downarrow} = \sum_{\alpha=1}^{n_d} L_\alpha Y^{-}_{\alpha} e^{-k_\alpha \Delta} + M_\alpha Y^{+}_{\alpha} + G^{\downarrow}(\mu_0). \tag{B4}$$

Here, $\mu_\alpha, c_\alpha, \alpha = 1, \ldots n_d$ are the discrete-ordinate quadrature values, $I^{\downarrow}$ is the downwelling intensity field at the surface expressed in terms of homogeneous solutions $Y^{\pm}_{\alpha}, k_\alpha$ in the lowest layer of the ~~atmopshere~~atmosphere, particular solutions $G^{\downarrow}(\mu_0)$ in that layer, and integration constants $L_\alpha, M_\alpha$ for that layer as determined from the BVP solution $\mathbf{x}_1 = \mathbf{A}^{-1}\mathbf{B}$. This flux computation does not require any post-processing, nor any evaluations at other levels in the atmosphere.

## Appendix C Description of Look Up Tables

Processing of GLER using online radiative transfer calculations is not efficient for the OMI mission due to their computationally expensive nature. Instead, LUT interpolation is used for the OMI mission, which speeds up the calculations significantly. To calculate GLER, two separate LUT's were generated, one for the TOA radiances calculated to include geometry-dependent surface BRDF effects, and the other to derive LER from these radiances using the quantities $I_o$, $S_b$, and $T$, as described in 2.5. $I_o$, $S_b$, and $T$ depend only on viewing geometries and surface pressure, whereas the TOA radiance table additionally included dependencies on chlorophyll, wind speed, and wind direction. The LUT nodes for the TOA radiance table shown in Table 7 were chosen by analyzing TOA radiance as a function of each input parameter to keep the interpolation error below 0.5%.

Table 7: LUT Structure for TOA Radiance Calculations

| Parameter | Number of Nodes | Step Size | Range |
|---|---|---|---|
| Pressure | 9 | 20-110 | 541-1100hPa |
| Solar Zenith Angle | 42 | 2 | 0-86° |
| Viewing Zenith Angle | 38 | 2 | 0.001-74° |
| Relative Azimuth Angle | 48 | 2-5 | 0-180° |
| Chlorophyll | 24 | 0.003-3.0 | 0.01-10 mg m$^{-3}$ |
| Wind Speed | 21 | 0.2-5.0 | 0.4-50 m s$^{-1}$ |
| Wind Direction | 36 | 10 | 0-350° |

*Data availability.* GLER will be available at https://aura.gesdisc.eosdis.nasa.gov/data/Aura_OMI_Level2/. The OMI Level 1 data used for calculations of GLER are available at https://aura.gesdisc.eosdisc.nasa.gov/data/

Aura_OMI_Level1/ (last access: 11 April 2019). The OMI Level 2 Collection 3 data which include $NO_2$ and OMI pixel corner products are available at https://aura.gesdisc.eosdis.nasa.gov/data/Aura_OMI_Level2/ (last access: 11 April 2019). The OMI $O_2$-$O_2$ cloud product can be provided upon request of the co-authors.

*Author contributions.* ZF led the paper and evaluation efforts. ZF, DH, AV, and RS wrote the paper. ZF and DH designed the GLER analysis. WQ carried out aerosol implementation and VLIDORT related simulations. NK and JJ provided guidance throughout the development of the manuscript. All authors contributed to the editing of the manuscript. RS and AS developed the VLIDORT code used for the BRDF and radiance computations.

*Competing interests.* The authors declare that they have no conflict of interest.

*Acknowledgements.* Funding for this work was provided by NASA through Aura core team funding as well as the Aura project and Aura Science Team and Atmospheric Composition Modeling and Analysis Program managed by Kenneth Jucks and Barry Lefer. We thank Patricia Castellanos and GMAO for providing us with the assimilated aerosol dataset. We thank David Antoine for useful discussions and providing data on the bidirectional aspects of water-leaving radiance. Additionally, we thank the MODIS and OMI teams for providing the calibrated ~~data sets~~datasets.

## References


Ahn, C., Torres, O., and Jethva, H.: Assessment of OMI near-UV aerosol optical depth over land, J. Geophys. Res. Atmos., 119, 24572473, https://doi.org/10.1002/2013JD020188, 2014.

Austin, R.W., :The remote sensing of spectral radiance from below the ocean surface, Optical Aspects of Oceanography, edited by Jerlov, N.G., and Nielsen, E.S., Academic Press, 317-344, 1974.

Cetinic, I., McClain, C.R., and Werdell, P.J.: Pre-Aerosol, Clouds, and Ocean Ecosystem (PACE) Mission Science Definition Team Report, Volume 2, PACE Technical Report Series, 2018.

Cox, C. and Munk, W.: Statistics of the sea surface derived from sun glitter, J. Mar. Res. 13, 198-227, 1954.

Dave, J.V.: Effect of aerosol on the estimation of total ozone in an atmospheric column from the measurements of the ultraviolet radiance, J. Atmos. Sci., 35, 899-911, https://doi.org/10.1175/1520-0469(1978)035¡0899

Dobber, M., Kleipool, Q., Dirksen, R., Levelt, P., Jaross, G., Taylor, S., Kelly, T., Flynn, L., Leppelmeier, G., and Rozemeijer, N.: Validation of Ozone Monitoring Instrument level 1b data products, J. Geophys. Res, 113, D15S06, https://doi.org/10.1029/2007JD008665, 2008.

Frouin, R., Schwindling, M., and Deschamps, P.Y.: Spectral reflectance of sea foam in the visible and near infrared: In situ measurements and remote sensing implications, J. Geophys. Res., 101, 14,36114,371, 1996.

Gelaro, R., McCarty, W., Surez, M.J., Todling, R., Molod, A., Takacs, L., Randles, C.A., Darmenov, A., Bosilovich, M.G., Reichle, R., Wargan, K., Coy, L., Cullather, R., Draper, C., Akella, S., Buchard, V., Conaty, A., da Silva, A.M., Gu, W., Kim, G., Koster, R., Lucchesi, R., Merkova, D., Nielsen, J.E., Partyka, G., Pawson, S., Putman, W., Rienecker, M., Schubert, S.D., Sienkiewicz, M., and Zhao, B.: The Modern-Era Retrospective Analysis for Research and Applications, Version 2 (MERRA-2). J. Climate, 30, 54195454, https://doi.org/10.1175/JCLI-D-16-0758.1, 2017.

Gordon, H.R.: Can the LambertBeer law be applied to the diffuse attenuation coefficient of ocean water?, Limn. and Oc., 34, 1389-1409, https://doi.org/10.4319/lo.1989.34.8.1389, 1989.

Gordon, H.R., Wang M.: Retrieval of water-leaving radiance and aerosol optical thickness over the oceans with SeaWiFS: A preliminary algorithm, Appl. Opt., 33, 443-452, https://doi.org/10.1364/AO.33.000443, 1994.

Hale, G. M., and Querry, M.R..: Optical constants of water in the 200 nm to 200 µ wavelength region, Appl. Opt., 12, 555-563, https://doi.org/10.1364/AO.12.000555, 1973.

Hu, C., Lee, Z., and Franz, B.: Chlorophyll-a algorithms for oligotrophic oceans: A novel approach based on three-band reflectance difference, J. Geophys. Res., 117, C01011, https://doi.org/10.1029/2011JC007395, 2012.

Imaoka, K., Maeda, T., Kachi, M., Kasahra, M., Ito, N., and Nakagawa, K.: Status of AMSR2 instrument on GCOM-W1, Proceedings of SPIE, 8528, 852815, https://doi.org/10.1117/12.977774, 2012.

Jaross, G. and Warner, J.: Use of Antarctica for validating reflected solar radiation measured by satellite sensors, J. Geophys. Res., 113, D16S34, https://doi.org/10.1029/2007JD008835, 2008.

Joiner, J.: OMI/Aura and MODIS/Aqua Merged Cloud Product 1-Orbit L2 Swath 13x24 km V003, Greenbelt, MD, USA, Goddard Earth Sciences Data and Information Services Center (GES DISC), Accessed: [June 3, 2019], https://disc.gsfc.nasa.gov/datacollection/OMMYDCLD_003.html, 2014

Kaufman, Y., Remer, L., Tanr, D., Li, R., Kleidman, R., Mattoo, S., Levy, R., Eck, T., Holben, B., Ichoku, C., Martins, J., and Koren, I.: A critical examination of the residual cloud contamination and diurnal sampling effects on MODIS estimates of aerosol over ocean, IEEE Trans. Geosci. Rem. Sens. 43, 2886-2897,

https://doi.org/10.1109/TGRS.2005.858430, 2006.

Kay, S., Hedley, J.D., and Lavender, S.: Sun glint correction of high and low spatial resolution images of aquatic scenes: a review of methods for visible and near-Infrared wavelengths, Rem. Sens., 1, 697-730, https://doi.org/10.3390/rs1040697, 2009.

Kleipool, Q. L., Dobber, M. R., de Haan, J. F., and Levelt, P. F.: Earth surface reflectance climatology from 3 years of OMI data, J. Geophys. Res., 113, D18308, https://doi.org/10.1029/2008jd010290, 2008.

Koelemeijer, R.B.A., Stammes, P., Hovenier, J.W., and de Haan, J.F.: A fast method for retrieval of cloud parameters using oxygen A-band measurements from the Global Ozone Monitoring Experiment, J. Geophys. Res., 106, 3475-3496, https://doi.org/10.1029/2000JD900657, 2001.

Koelemeijer, R.B.A., de Haan, J.F., and Stammes, P.:A database of spectral surface reflectivity in the range 335772 nm derived from 5.5 years of GOME observations, J. Geophys. Res., 108, 4070, doi:10.1029/2002JD002429, 2003.

Krotkov, N. A., Lamsal, L. N., Celarier, E. A., Swartz, W. H., Marchenko, S. V., Bucsela, E. J., Chan, K. L., Wenig, M., and Zara, M.: The version 3 OMI $NO_2$ standard product, Atmos. Meas. Tech., 10, 3133-3149, https://doi.org/10.5194/amt-10-3133-2017, 2017.

Lamsal, L. N., Krotkov, N. A., Celarier, E. A., Swartz, W. H., Pickering, K. E., Bucsela, E. J., Gleason, J. F., Martin, R. V., Philip, S., Irie, H., Cede, A., Herman, J., Weinheimer, A., Szykman, J. J., and Knepp, T. N.: Evaluation of OMI operational standard $NO_2$ column retrievals using in situ and surface-based $NO_2$ observations, Atmos. Chem. Phys., 14, 1158711609, https://doi.org/10.5194/acp-14-11587-2014, 2014.

Lee, Z.P., Du, K.P., and Arnone, R.: A model for the diffuse attenuation coefficient of downwelling irradiance, J. Geophys. Res., 110, C02016, http://doi.org/10.1029/2004JC002275, 2005.

~~Lee, C., Martin, R.V., van Donkelaar, A., O'Byrne, G., Krotkov, N., Richter, A., Huey, L.G., and Holloway, J.S.: Retrieval of vertical columns of sulfur dioxide from SCIAMACHY and OMI: Air mass factor algorithm development, validation, and error analysis, J. Geophys. Res., 114, D22303, doi:10.1029/2009JD012123, 2009.~~

Lee, Z., Hu, C., Shang, S., Du, K., Lewis, M., Arnone, R., and Brewin, R.: Penetration of UVvisible solar radiation in the global oceans: Insights from ocean color remote sensing, J. Geophys. Res. Oceans, 118, 4241 4255, https://doi.org/10.1002/jgrc.20308, 2013.

Lee, Z., Wei, J., Voss, K., Lewis, M., Bricaud, A., and Huot, Y.: Hyperspectral absorption coefficient of "pure" seawater in the range of 350-550 nm inverted from remote sensing reflectance, Appl. Opt., 54, 546-558, https://doi.org/10.1364/AO.54.000546, 2015.

Lee, Z. and Hu, C.: Global distribution of Case-1 waters: An analysis from SeaWiFS measurements. Rem. Sens. Environ., 101, 270-276, https://doi.org/10.1016/j.rse.2005.11.008, 2006.

Levelt, P. F., Joiner, J., Tamminen, J., Veefkind, J. P., Bhartia, P. K., Stein Zweers, D. C., et al.: The Ozone Monitoring Instrument: Overview of 14 years in space. Atmos. Chem. and Phys., 18, 56995745, https://doi.org/10.5194/acp-18-5699-2018, 2018.

Lucchesi, R.: File Specification for GEOS-5 FP-IT. GMAO Office Note No. 2 (Version 1.2), 60pp, available from http://gmao.gsfc.nasa.gov/pubs/office_notes, 2013.

Menzel, W., Frey, R., Zhang, H., Wylie, D., Moeller, C., Holz, R., Maddux, B., Baum, B., Strabala, K., and Gumley, L.: MODIS global cloud-top pressure and amount estimation: algorithm description and results. J.

Appl. Meteor. Climatolol., 47, 1175-1198, https://doi.org/10.1175/2007JAMC1705.1, 2007.

Mishchenko, M. I. and Travis, L. D.: Satellite retrieval of aerosol properties over the ocean using polarization as well as intensity of reflected sunlight, J. Geophys. Res., 102, 16,989-17,013, https://doi.org/10.1029/96JD02425, 1997.

Moore, T. S., Campbell, J. W., Dowell, M. D.: A class-based approach to characterizing and mapping the uncertainty of the MODIS ocean chlorophyll product, Rem. Sens. Environ., 113, 2424-2430, https://doi.org/10.1016/j.rse.2009.07.016, 2009.

Morel, A.: Optical modeling of the upper ocean in relation to its biogeneous matter content (Case I waters), J. Geophys. Res., 93, 10749-10768, https://doi.org/10.1029/JC093iC09p10749, 1988.

Morel, A. and Gentili, B.: Diffuse reflectance of oceanic waters : its dependence on sun angles as influenced by molecular scattering contribution. Appl. Optics, 30, 4427-4438, https://doi.org/10.1364/AO.30.004427, 1991.

Morel, A. and Gentili, B.: Bidirectional reflectance of oceanic waters: accounting for Raman emission and varying particle scattering phase function. Appl. Optics, 41, 6289-6306, https://doi.org/10.1364/AO.41.006289, 1992.

Morel, A. and Gentili, B.: Diffuse reflectance of oceanic waters (2) : bidirectional aspects. Appl. Optics, 32: 6864-6879, https://doi.org/10.1364/AO.32.006864, 1993.

Morel, A. and Gentili, B.: Diffuse reflectance of oceanic water. III. Implication of bidirectionality for the remote-sensing probe, Appl. Opt., 35, 4850-4862, https://doi.org/10.1364/AO.35.004850, 1996.

Morel, A., Antoine, D., and Gentili, B.: Bidirectional reflectance of oceanic waters: Accounting for Raman emission and varying particle scattering phase function, Appl. Opt., 41, 62896306, https://doi.org/10.1364/AO.41.006289, 2002.

Morel, A., Gentili, B., Claustre, H., Bricaud, A., Ras, J., and Tiche, F.: Optical properties of the clearest natural waters. Limnol. Oceanogr., 20, 177-184 https://doi.org/10.4319/lo.2007.52.1.021, 2007.

Morel, A., and Maritorena, S.: Bio-optical properties of oceanic waters: A reappraisal, J. Geophys Res., 106, 7163-7180, https://doi.org/10.1029/2000JC000319, 2001.

Morel, A., and Gentili, B.: A simple band ratio technique to quantify the colored dissolved and detrital organic material from ocean color remotely sensed data, Rem. Sens. Environ., 113, 998-1011, https://doi.org/10.1016/j.rse.2009.01.008, 2009.

Nazaryan, H., McCormick, M. P., and Menzel, W. P.: Global characterization of cirrus clouds using CALIPSO data, J. Geophys. Res., 113, D16211, https://doi.org/10.1029/2007JD009481, 2008.

Park, Y. and Rudick, M.: Model of remote-sensing reflectance including bidirectional effects for case 1 and case 2 waters, Appl. Opt. 44, 1236-1249, https://doi.org/ 10.1364/AO.44.001236, 2005.

Pope, R. M., and E. S. Fry. Absorption spectrum (380-700nm) of pure water. II. Integrating cavity measurements, Appl. Opt., 36, 8710-8723, https://doi.org/10.1364/AO.36.008710, 1997.

Qin, W., Fasnacht, Z., Haffner, D., Vasilkov, A., Joiner, J., Krotkov, N., Fisher, B., and Spurr, R.: A geometry-dependent surface Lambertian-equivalent reflectivity product at 466nm for UV/Vis retrievals: Part 1. Evaluation over land surfaces using measurements from OMI, Atmos. Meas. Tech., https://doi.org/10.5194/amt-2018-327, in press, 2019.

Quickenden, T. I., and Irvin, J. A.: The ultraviolet absorption spectrum of liquid water, J. Chem. Phys., 72,

4416-4428, https://doi.org/10.1063/1.439733, 1980.

Randles, C.A., Silva, A.M.D., Buchard, V., Colarco, P.R., Darmenov, A., Govindaraju, R.,Smirnov, A., Holben, B., Ferrare, R., Hair, J., Shinozuka, Y., Flynn, C.J.,: The MERRA-2 aerosol reanalysis, 1980 onward. Part I: system description and data assimilation evaluation. J. Clim. 30, 68236850, https://doi.org/10.1175/JCLI-D-16-0609.1, 2017.

Sayer, A. M., Thomas, G. E., and Grainger, R. G.: A sea surface reflectance model for (A)ATSR, and application to aerosol retrievals. Atmos. Meas. Tech., 3, 813838, https://doi.org/10.5194/amt-3-813-2010, 2010.

Sayer, A. M., Hsu, N. C., Bettenhausen, C., Ahmad, Z., Holben, B. N., Smirnov, A., Thomas, G. E., and Zhang, J.: SeaWiFS Ocean Aerosol Retrieval (SOAR): Algorithm, validation, and comparison with other data sets, J. Geophys. Res., 117, D03206, https://doi.org/10.1029/2011JD016599, 2012.

Sayer, A. M., Hsu, N. C., Bettenhausen, C., Holz, R. E., Lee, J., Quinn, G., and Veglio, P.: Cross-calibration of S-NPP VIIRS moderate-resolution reflective solar bands against MODIS Aqua over dark water scenes, Atmos. Meas. Tech., 10, 1425-1444, https://doi.org/10.5194/amt-10-1425-2017, 2017.

Schaepman-Strub, G., Schaepman, M. E., Painter, T. H., Dangel, S., Martonchik, J. V.: Reflectance quantities in optical remote sensing: definitions and case studies, Rem. Sens. Environ., 103, 27-42, https://doi.org/10.1016/j.rse.2006.03.002, 2006.

Schenkeveld, V. M. E., Jaross, G., Marchenko, S., Haffner, D., Kleipool, Q. L., Rozemeijer, N. C., Veefkind, J. P., and Levelt, P. F.: In-flight performance of the Ozone Monitoring Instrument, Atmos. Meas. Tech., 10, 1957-1986, https://doi.org/10.5194/amt-10-1957-2017, 2017.

Seftor, C. J., Taylor, S. L., Wellemeyer, C. G., and McPeters, R. D.: Effect of Partially-Clouded Scenes on the Determination of Ozone, in: Ozone in the Troposphere and Stratosphere, Part 1, Proceedings of the Quadrennial Ozone Symposium, Charlottesville, USA, 1992, NASA Conference Publication 3266, 919922, 1994.

Spurr, R. J. D.: VLIDORT: a linearized pseudo-spherical vector discrete ordinate radiative transfer code for forward model and retrieval studies in multilayer multiple scattering media, J. Quant. Spectr. Rad. Trans., 102, 316-421, https://doi.org/10.1016/j.jqsrt.2006.05.005, 2006.

Spurr, R., Stamnes, K., Eide, H., Li, W., Zhang, K. and Stamnes, J.: Simultaneous Retrieval of Aerosols and ocean properties: A classic inverse modeling approach. I. Analytic jacobians from the Linearized CAO-DISORT model, J. Quant. Spectr. Rad. Trans., https://doi.org/ 10.1016/j/jqsrt.2006.09.009, 2007.

Spurr, R, and M. Christi, The LIDORT and VLIDORT Linearized Scalar and Vector Discrete Ordinate Radiative Transfer Models: Updates in the last 10 Years. Light Scattering Reviews, Volume 12, ed. A. Kokhanovsky, Springer, 2019.

Stammes, P., Sneep, M., de Haan, J.F., Veefkind, J.P., Wang, P., and Levelt, P.F.: Effective cloud fractions from the Ozone Monitoring Instrument: Theoretical framework and validation, J. Geophys. Res., 113, D16S38, https://doi.org/10.1029/2007JD008820, 2008.

Szeto, M., Werdell, P. J., Moore, T. S., and Campbell, J. W.: Are the world's oceans optically different?, J. Geophys. Res., 116, C00H04, https://doi.org/10.1029/2011JC007230, 2011.

Thomas , G. and Stamnes, K.: Radiative transfer in the atmosphere and ocean. New York, NY, Cambridge University Press, 1999.

Tilstra, L. G., Tuinder, O. N. E., Wang, P., and Stammes, P.: Surface reflectivity climatologies from UV to NIR

determined from Earth observations by GOME-2 and SCIAMACHY, J. Geophys. Res., 122, 4084-4111, https://doi.org/10.1002/2016JD025940, 2017.

Torres, O., Bhartia, P., Herman, J., Ahmad, Z., and Gleason, J.: Derivation of aerosol properties from satellite measurments of backscattered ultraviolet ratiadtion: Theoretical basis, J. Geophys. Res., 110, D14, https://doi.org/10.1029/98JD00900, 1998.

Torres, O., Tanskanen, A., Veihelman, B., Ahn, C., Braak, R., Bhartia, P. K., Veefkind, V., and Levelt, P.: Aerosols and surface UV products from OMI observations: an overview, J. Geophys. Res., 112, D24S47, https://doi.org/10.1029/2007JD008809, 2007.

Vasilkov, A. P., Herman, J., Krotkov, N. A., Kahru, M., Mitchell, B. G., and Hsu, C.: Problems in assessment of the UV penetration into natural waters from space-based measurements, Opt. Eng., 41, 30193027, https://doi.org/10.1117/1.1516822, 2002.

Vasilkov, A., Joiner, J., Bhartia, P., Levelt, P., and Stephens, G.: Evaluation of the OMI cloud pressured derived from the rotational Raman scattering by comparisons with other satellite data and radiative transfer simulations, J. Geophys., Res., 113, D15S19, https://doi.org/10.1029/2007D008689, 2008.

Vasilkov, A. P., Herman, J. R., Ahmad, Z., Karu, M., and Mitchell, B. G.: Assessment of the ultraviolet radiation field in ocean waters from space-based measurements and full radiative-transfer calculations, Appl. Opt., 44, 2863-2869, https://doi.org/812 10.1364/AO.44.002863, 2005.

Vasilkov, A. P., Qin, W., Krotkov, N., Lamsal, L., Spurr, R., Haffner, D., Joiner, J., Yang, E.-S., and Marchenko, S.: Accounting for the effects of surface BRDF on satellite cloud and trace-gas retrievals: a new approach based on geometry-dependent Lambertian equivalent reflectivity applied to OMI algorithms, Atmos. Meas. Tech., 10, 333-349, https://doi.org/10.5194/amt-10-333-2017, 2017.

Vasilkov, A. P., Yang, E.-S., Marchenko, S., Qin, W., Lamsal, L., Joiner, J., Krotkov, N., Bhartia, P. K. and Spurr, R.: A cloud algorithm based on the $O_2$-$O_2$ 477 nm absorption band featuring an advanced spectral fitting method and the use of surface geometry-dependent Lambertian-equivalent reflectivity, Atmos. Meas. Tech., 11, 4093-4107, https://doi.org/10.5194/amt-11-4093-2018, 2018.

Veefkind, J. P., de Haan, J. F., Sneep, M., and Levelt, P. F.: Improvements to the OMI ($O_2$-$O_2$) operational cloud algorithm and comparisons with ground-based radar-lidar observations, Atmos. Meas. Tech., 9, 6035-6049, https://doi.org/10.5194/amt-9-6035-2016, 2016.

Wentz, F. J., Meissner, T.: AMSR-E/Aqua L2B Global Swath Ocean Products Derived from Wentz Algorithm V002 (January 2009, June to August 2010). Updated daily. Boulder, Colorado USA: National Snow and Ice Data Center. Digital media, 2004.

Wentz, F.J., and Meissner, T.: AMSR Ocean Algorithm Theoretical Basis Document, Version 2, Remote Sensing Systems, Santa Rosa, CA, 2000.

Wentz, F. and Meissner, T.: Supplement 1: Algorithm theoretical basis document for AMSR-E ocean algorithms. Santa Rosa, CA: Remote Sensing Systems, 2007.

Wentz, F., Hilburn, K., and Smith, K.: RSS SSMIS ocean product grids daily from DMSP F16 NETCDF. Dataset available online from the NASA Global Hydrology Resource Center DAAC, Huntsville, Alabama, USA. https://doi.org/10.5067/MEASURES/DMSFP-F16/SSMIS/DATA301

Werdell, P. J., Behrenfeld, M. J., Bontempi, P. S., Boss, E., Cairns, B., Davis, G. T., Franz, B. A., Gliese, U. B., Gorman, E. T., Hasekamp, O., Knobelspiesse, K. D., Mannino, A., Martins, J. V., McClain, C. R., Meister,

G., and Remer, L. A.: The Plankton, Aerosol, Cloud, Ocean Ecosystem Mission: Status, Science, Advances, Bull. Amer. Meteor. Soc., 100, 1775-1794, https://doi.org/10.1175/BAMS-D-18-0056.1, 2019.

Westberry, T. K., Boss, E., and Lee, Z.: Influence of Raman scattering on ocean color inversion models, Appl. Opt., 52, 5552-5561, https://doi.org/10.1364AO/52.005552, 2013.

Zhang, X., L. Hu, and M.-X. He.: Scattering by pure seawater: Effect of salinity, Opt. Express., 17, 5698-5710, https://doi.org/10.1364/OE.17.005698, 2009.

Zhou, Y., Brunner, D., Spurr, R. J. D., Boersma, K. F., Sneep, M., Popp, C., and Buchmann, B.: Accounting for surface reflectance anisotropy in satellite retrievals of tropospheric $NO_2$, Atmos. Meas. Tech., 3, 1185-1203, https://doi.org/10.5194/amt-3-1185-2010, 2010.